Linear Collider Collaboration Tech Notes

NLC Damping Ring Wiggler Studies 1999

December 3, 1999

J. Corlett, N. Hartmann, K. Kennedy, G. Koehler, S. Marks, J. Rasson, T. Saleh
Lawrence Berkeley National Laboratory
Berkeley, CA, USA

Abstract:

The primary objective of FY99 was to develop credible conceptual wiggler requirements. Three magnet technologies were considered: electromagnet, hybrid permanent magnet and superconducting. Based upon an early assessment of requirements, a hybrid magnet similar to existing designs, with appropriate modification of gap and period, satisfies basic requirements. However, radiation damage is potentially a serious problem for the ND-FE-B permanent magnet material, and cost remains an issue for samarium cobalt magnets. Therefore the primary effort was put into developing a radiation-hard electromagnet wiggler conceptual design that has the same performance. A qualitative discussion of the advantages and disadvantages of the various technologies is presented

NLC Damping rings wiggler studies 1999

J. Corlett, N. Hartman, K. Kennedy , G. Koehler, S. Marks, J. Rasson, T. Saleh
Lawrence Berkeley National Laboratory
Berkeley, CA 94720

Contents

1.0 Summary

The primary objective for FY99 was to develop a credible conceptual wiggler design that meets NLC main electron and positron damping ring physics requirements. Three magnet technologies were considered: electromagnet, hybrid permanent magnet, and superconducting. Based upon an early assessment of requirements, a hybrid magnet similar to existing designs, with appropriate modification of gap and period, satisfies basic requirements. However, radiation damage is potentially a serious problem for the Nd-Fe-B permanent magnet material, and cost remains an issue for samarium cobalt

magnets. Therefore the primary effort was put into developing a radiation hard electromagnet wiggler conceptual design that has the same performance. A qualitative discussion of the advantages and disadvantages of the various technologies is given below.

1.1 Requirements

The design objective for the wigglers is to maximize the energy loss within the wigglers, which is proportional to the integrated magnetic induction squared,

$$I_B^2 = \int B^2 \, dz$$

while minimizing the quantum excitation, which is proportional to $B^{3/2}$. The current NLC lattice design requires a total value for I_B^2 of 106 T-m^2. Wigglers are to be arranged in a single FODO lattice straight, occupying one of the two long straights in the main damping rings [1].

1.1.1 Reference design parameters

Physics studies were initially based upon the following wiggler parameters, which were extrapolated from characteristics of the SSRL BL9 hybrid wiggler [2]:

- B_w = 2.15 T (sinusoidal field)
- λ_w = 0.27 m
- magnet gap, g = 2.0 cm
- number of wiggler sections, N_s = 20
- length of wiggler sections, L_s = 2.194 m
- distance between quadrupole centers, L_q = 2.41 m
- total length of straight, L_{st} = 58 m

From these parameters, we have developed a baseline design which will be described here.

2.0 Magnet technology options

Three magnet technology options were considered: electromagnet, hybrid permanent magnet, and superconducting. The advantages and disadvantages are summarized in the table below. The dominant points for each technology are underlined.

	Advantages	Disadvantages
Electromagnet	• Standard technology • Easy to turn off, tune field • Radiation tough • Relatively low initial cost	• Consumes power • Complicated connections • Narrow lateral field distribution
Hybrid	• Does not require power • Well tested in light sources	• Must move to turn off • Subject to radiation damage • Field varies with temperature • Relatively high initial cost
Superconducting	• Shorter straight • Larger gap	• Cryogenic infrastructure • Non-standard technology • Costly • Uncertain reliability

The NLC damping ring will be a high radiation environment, with 120 Hz injection/extraction cycles and a kW-level beam power injector. The vacuum chamber through the wiggler section is likely to be the limiting aperture. Therefore, the issue of potential radiation induced demagnetization of permanent magnet blocks is serious. A hybrid wiggler using Nd-B-Fe permanent magnets would require upstream beam collimation to limit the radiation within the straight. This adds complexity and cost to the ring design. The radiation issue as well as the overall initial costs were the primary motivations for the development of a viable electromagnet design, which is now our baseline design.

3.0 Electromagnet design

The pole geometry for this magnet is unconventional compared to a wiggler designed for use in a synchrotron light source. The design objective for a light source wiggler is generally to maximize the peak field. This is most effectively accomplished for an electromagnet by tapering the pole in both the beam (z) and transverse (x,y) directions. This will however produce a sharply peaked field profile that does not effectively maximize I_B^2.

Figure 1 below shows a single period of the electromagnet design developed to meet the physics requirements. The pole is square and long in the beam direction in order to maximize I_B^2. However, in order to minimize the effects of magnet saturation that would normally occur for a square pole, the pole is narrow at the base and is strongly tapered in the direction transverse to the beam direction. Saturation is further reduced by placement

of Sm-Co permanent magnet blocks in the pocket left by the pole taper. (Note that while Sm-Co material is weaker magnetically than Nd-Fe-B, it is more radiation tough). The magnet orientation is chosen to reverse bias the pole flux. A coil is wrapped around the pole and block assembly. The coil is removed from the first pole of Figure 1 to show the pole and permanent magnet block configuration.

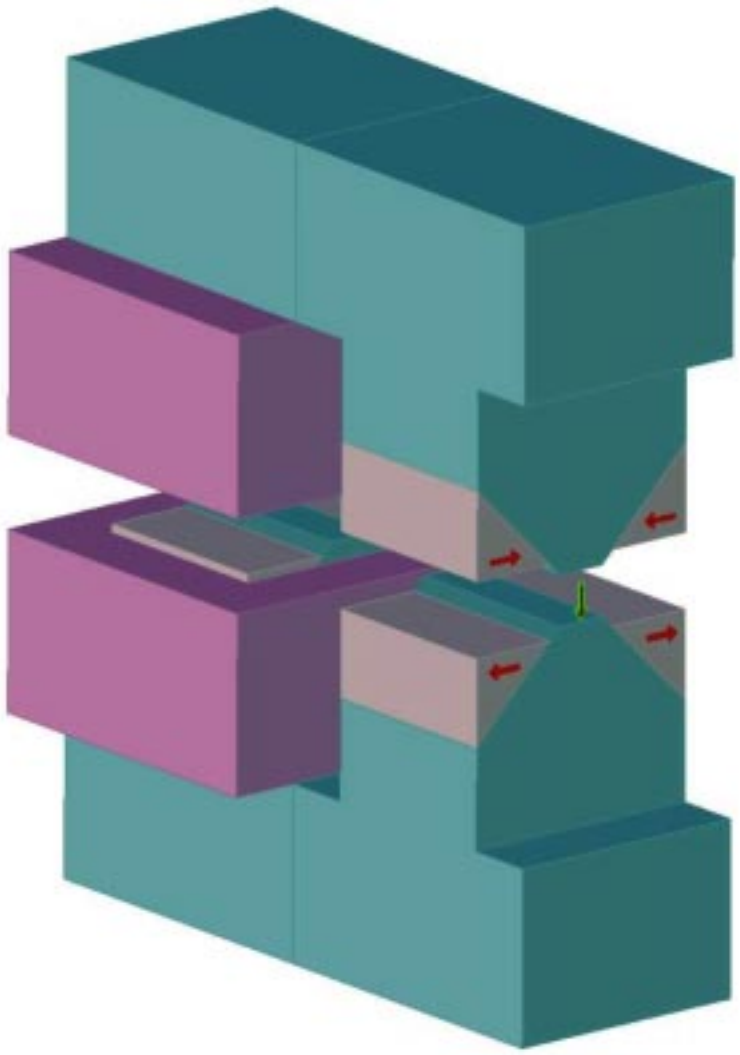

Figure 1. Electromagnet wiggler, one period.

The width of the pole tip is chosen to give a peak field corresponding to 98% of that for an infinitely wide pole. This minimizes the flux entering the bottom pole surface without sacrificing the peak field and thus I_B^2 on the axis. Because of the high on-axis field and the consequent flux entering the pole tip, the pole tip will be saturated. Additional flux that enters the lateral pole surfaces would result in increasing flux density beyond the

pole tip for an untapered pole. The pole taper, in conjunction with the reverse flux bias provided by the permanent magnets, results in a manageable flux density beyond the immediate pole tip. Sm-Co permanent magnet material has been chosen for this purpose because it is relatively radiation tough compared to Nd-Fe-B.

The issue of pole saturation relates directly to the current required to achieve the desired field. The desired field together with the pole geometry fixes the required current. The fixed period length together with the limited capacity for coil cooling place constraints upon the maximum allowed current density. For a fixed current, the required power is proportional to current density. The objective of minimizing power and cooling requirements conflicts with the desire to concentrate current near the pole tip to reduce pole flux, and thus pole saturation.

Several coil configurations were examined for a 27 cm period with the pole shape shown in Figure 1. Figure 2, which plots on-axis B^2 distributions, provides a summary of the results for configuration labeled D0, D1, D2, D3, D4, and D5. The configurations differ in pole material, use of permanent magnets, coil geometry, current density and required power. D0 corresponds to the 2.15T sinusoidal physics reference (section 1.1.1). The shape of the B^2 distributions for D1 through D5 are the same because they share the same pole shape; the different coil, permanent magnet and pole material configurations affect the power, current density and peak field. The total current is the same, 22000 Amp-turns, for D1 through D5.

Figure 3 shows lateral and axial cross sections for configurations D1, D2 and D3. Each of these use vanadium permandur pole material with the coil occupying the pocket left by the pole taper. Therefore, they do not include a permanent magnet insert. They differ only by current density. D1 has a high current density coil. It achieves 99% of the target I_B^2 value with a current density of 2000 A/cm^2 and an electrical power requirement of 50 kW per meter of wiggler.

The coil for D2 is modified so that the first 1 cm of coil near the pole tip has a current density of 2000 A/cm^2; the remainder of the coil has a current density of 1000 A/cm^2. The idea for this configuration is to concentrate the current at the pole tip where it does the most to reduce pole saturation, but to reduce the current density elsewhere to reduce the power requirement and to ease the cooling requirement. This achieves 97% of the target I_B^2 with a power requirement of 32 kW per meter of wiggler. The decreased current density requires a larger coil to carry the same total current. The pole and return yoke must also be extended to accommodate the larger coil. The coil and pole/yoke extensions are shown in Figure 3.

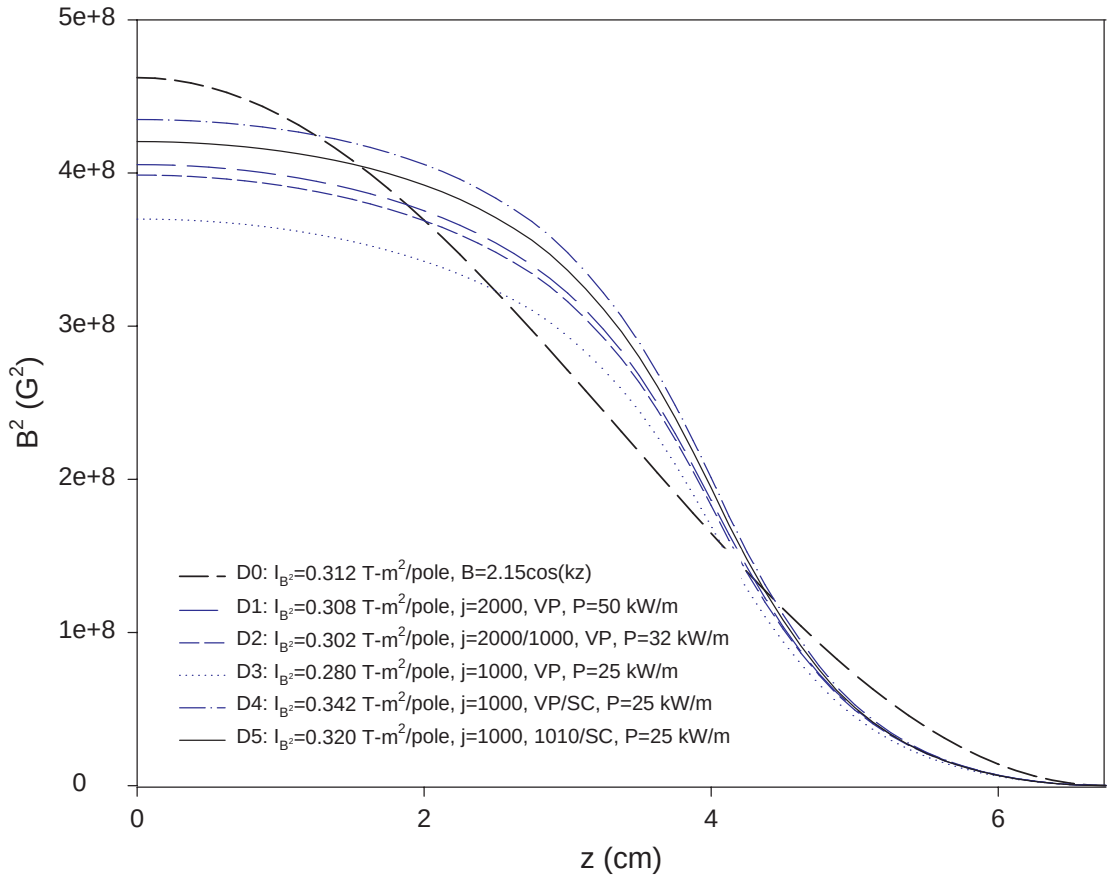

Figure 2. B^2 for several 27 cm period electromagnet designs.

The coil for D3 has a uniform current density of 1000 A/cm^2, thus requiring additional coil and pole/yoke extensions. This current density level is fairly routine for cooled magnet coils. This configuration achieves 90% of the target I_B^2 with a power requirement of 25 kW per meter of wiggler.

Configuration D4 uses the same pole/yoke configuration as D3. However, the coil is moved out of the taper pocket so that the coil is a simplified straight winding, with Sm-Co permanent magnets inserted into the pockets. This is the geometry illustrated in Figure 1. This configuration achieves 110% of the target I_B^2 value with the same 25 kW/m power required for D3. The additional cost and complexity associated with the Sm-Co inserts is offset by the simpler coil construction.

Configuration D5 differs from D4 only in pole material. Low carbon 1010 steel is used for the pole rather than vanadium permandur. Vanadium permandur saturates at a higher flux density than does 1010 steel, but with an increased material, machining and construction cost. The D4 configuration would require separate vanadium permandur poles be attached to a low carbon steel yoke assembly. The D5 configuration allows for

an entire pole/yoke assembly to be machined from a single low carbon steel blank. This should result in a significant cost reduction. D5 achieves 103% of the target I_B^2 value with 25 kW/m power.

The length of the wiggler sections is based upon using 10 sections total. Each wiggler includes 16 periods, or 32 full strength poles, with end transitions. The additional length for the two ends is estimated to be $2\lambda/3$; the total I_B^2 value for the ends is estimated to be 0.28 T-m^2. Trim windings will be incorporated into the end pole sections. The center-to-center distance between quadrupoles is based upon a layout which includes photon stops, pump ports, flanges, and bellows. The section length represents a minimum number of photon stops and quadrupoles in the straight in order to minimize the total length, and is determined by photon stop capacity. Note that quadrupole spacing is approximately double that used for initial physics studies. A final determination of the section length and quadrupole spacing must consider the consequences for the matching section.

Configuration D5 is the current baseline electromagnet design. The design characteristics are summarized below.

- B = 2.05 T (sinusoidal field)
- I_B^2 = 0.32 T-m^2/pole
- Wiggler period λ_w = 0.27 m
- magnet gap, g = 2.0 cm
- number of wiggler sections, N_s = 10
- length of wiggler sections, L_s = 4.51 m
- distance between quadrupole centers, L_q = 5.09 m
- total length of straight, L_{st} = 50.9 m

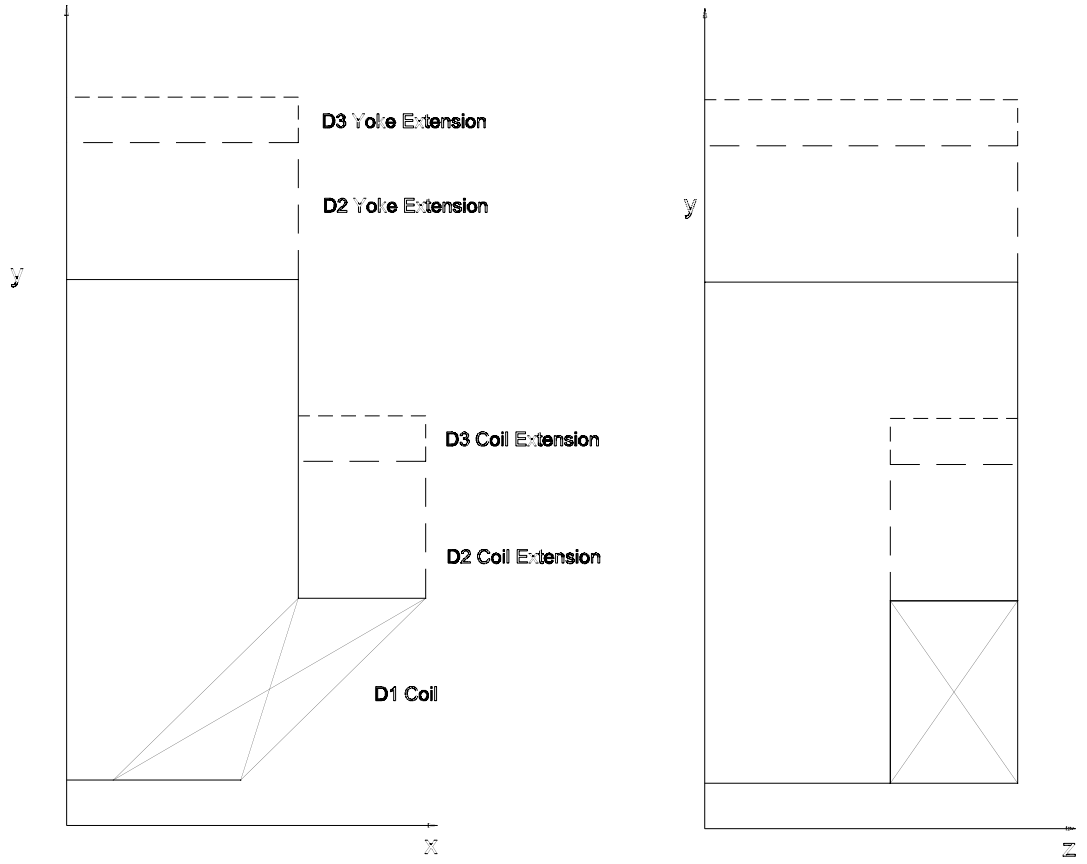

Figure 3. Configurations D1, D2, D3

3.1 Lateral Field Distribution

The narrow pole design developed for the electromagnet wiggler is very efficient in minimizing the effects of pole saturation while meeting the I_B^2 requirement with a modest power. However, the narrow pole tip results in a horizontal field roll-off that may have an effect on the storage ring dynamic aperture. The lateral field distribution for this pole design is shown in Figure 4. A field distribution is also shown for a pole modified by the addition of pole face bumps used to flatten the field distribution. The nominal amplitude of beam centroid motion in the wiggler is 0.59 mm. The field distributions shown in Figure 4 are the result of two dimensional field analysis. Figure 5 shows one half of the pole tip profile; the pole tip with bump is shown as a solid line, while the pole tip without bump is shown as a dashed line. Figure 4 demonstrates that the pole bump is effective in increasing the field distribution flatness; it does, however, come with a cost. The pole bump results in an increase in flux density near tip, thus requiring additional power for the same field. The estimated power increase is about 10%.

The lateral field roll-off will result in a deviation from ideal beam trajectory. Particle trajectories were calculated through wigglers with the two field distributions. Figures 6 through 9 plot trajectory deviation as a function of pole number, or wiggler length. The trajectories were calculated using lumped kicks at each pole. The entrance and exit poles have half strength kicks. Trajectory deviations are calculated by subtracting the particle wiggle and initial offset. The nominal wiggle amplitude is 0.59 mm.

Figure 6 corresponds to the pole without bumps for a range of entrance offset of $x_0 = \pm$ 0.05 cm, with no entrance angle ($x'_0 = 0$). Figure 7 corresponds to the same pole with an entrance angle range of $x'_0 = 0.05$ mrad, with an offset $x_0 = 0$. Figures 8 and 9 correspond to the pole with bumps. Figure 8 plots divergence for a range of entrance offset of $x_0 = \pm$ 0.05 cm, with no entrance angle ($x'_0 = 0$). Figure 9 plots divergence for an entrance angle range of $x'_0 = \pm$ 0.05 mrad, with an offset $x_0 = 0$. The perturbation from ideal trajectory with bumps is significantly reduced from the no-bump case. Note that the all plots show deviations out to a length of 100 poles. The nominal wiggler section (between quadrupoles) is 33 1/3 poles, including ends. Tailoring of the trim coil strength at the ends of wigglers can reduce these effects.

The beam dynamics impacts associated with these field profiles remains to be studied.

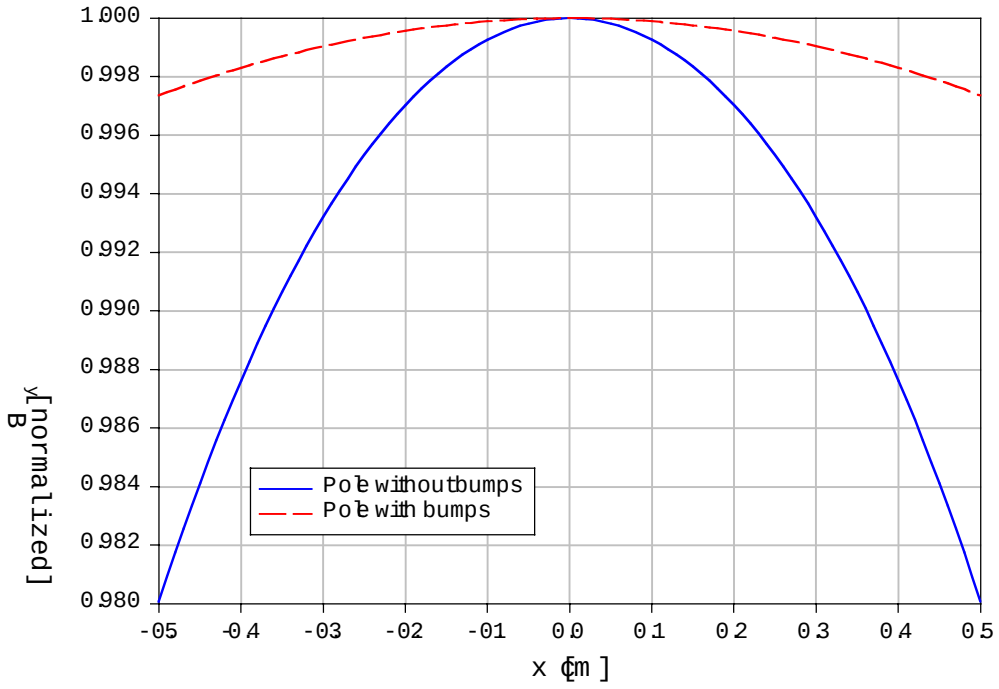

Figure 4. Lateral field distribution (normalized B) for D5 pole, and D5 pole with bumps.

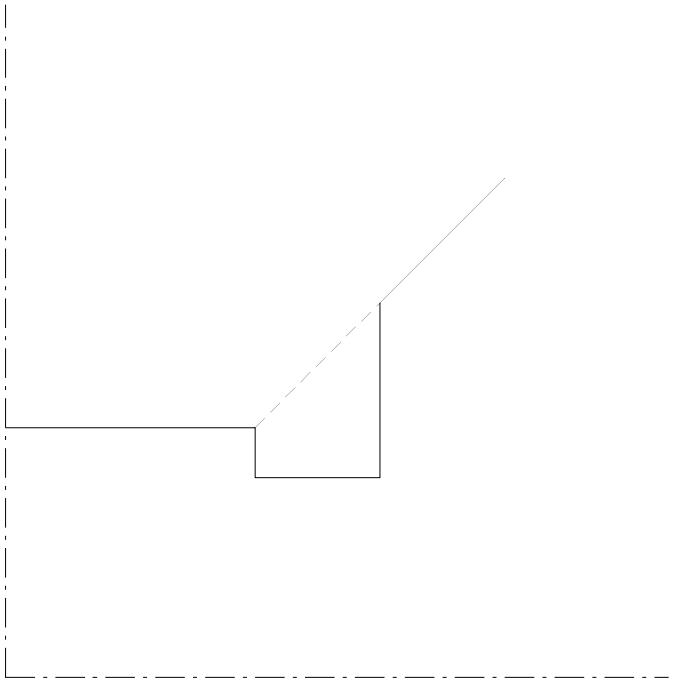

Figure 5. Pole tip bump.

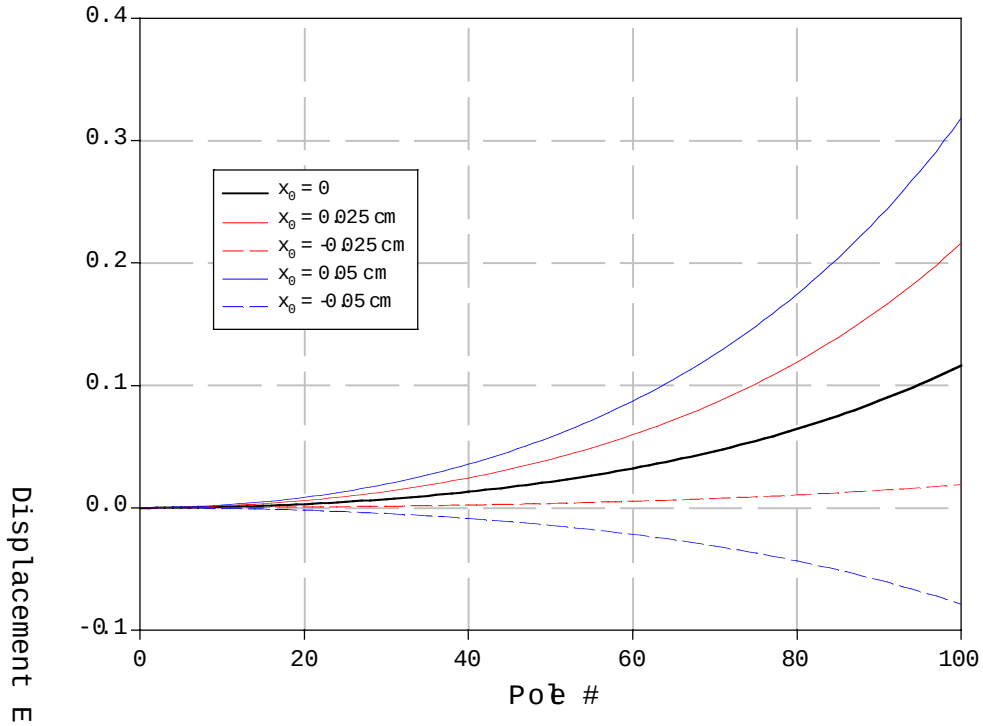

Figure 6. Trajectory deviations (cm) for pole without bumps, with $x_0' = 0$.

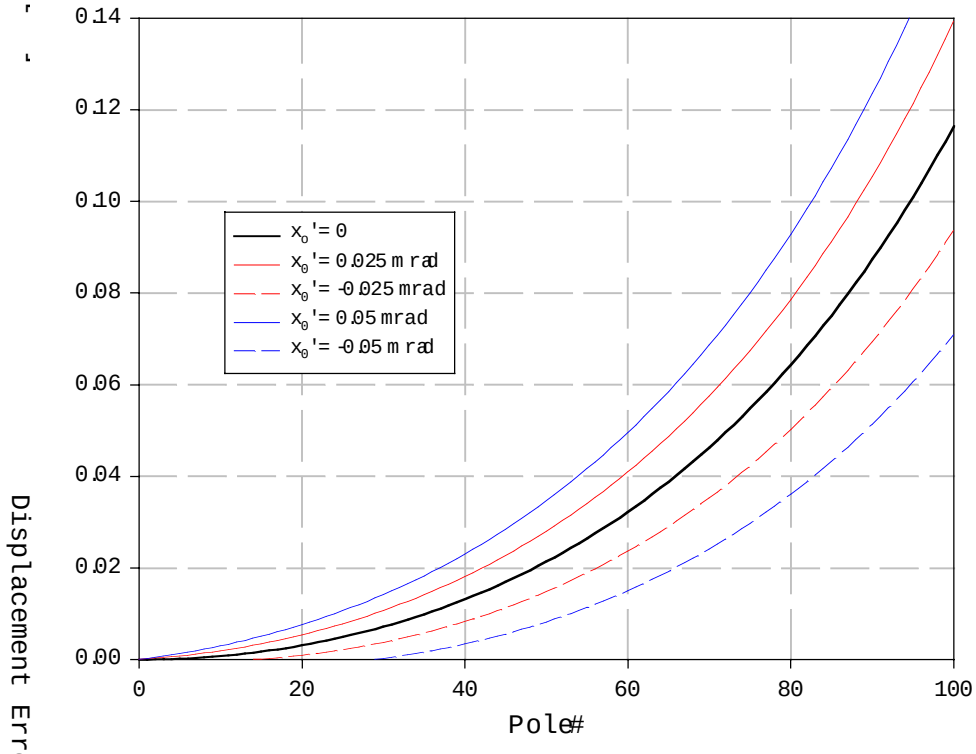

Figure 7. Trajectory deviations (cm) for pole without bumps, with $x_0 = 0$.

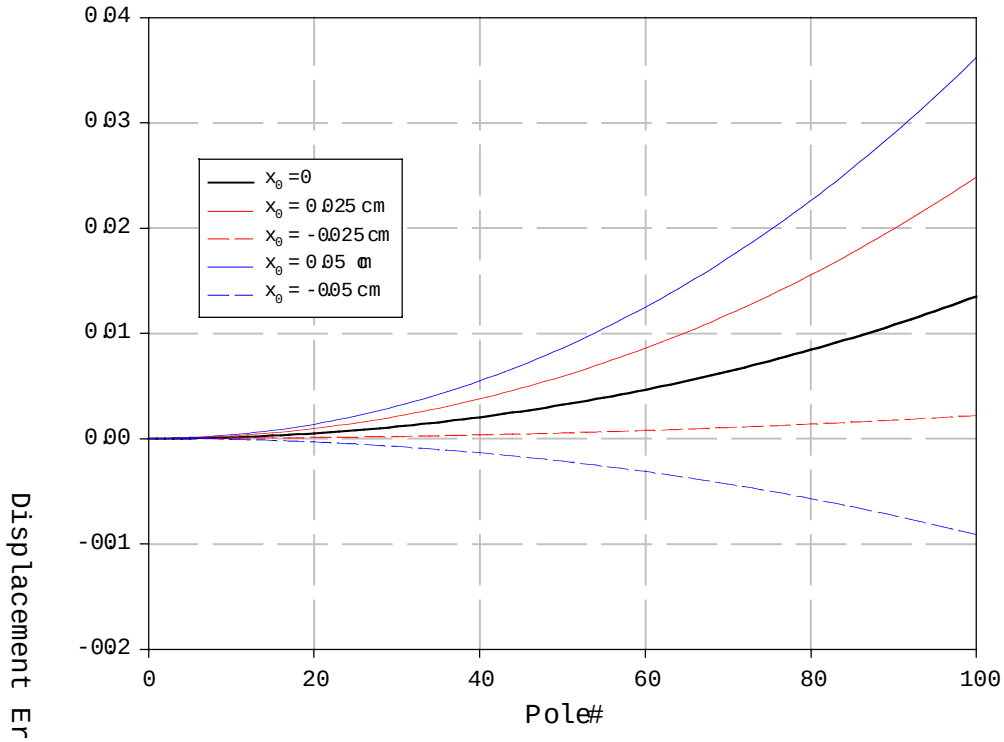

Figure 8. Trajectory deviations (cm) for pole with bumps, with $x_0' = 0$.

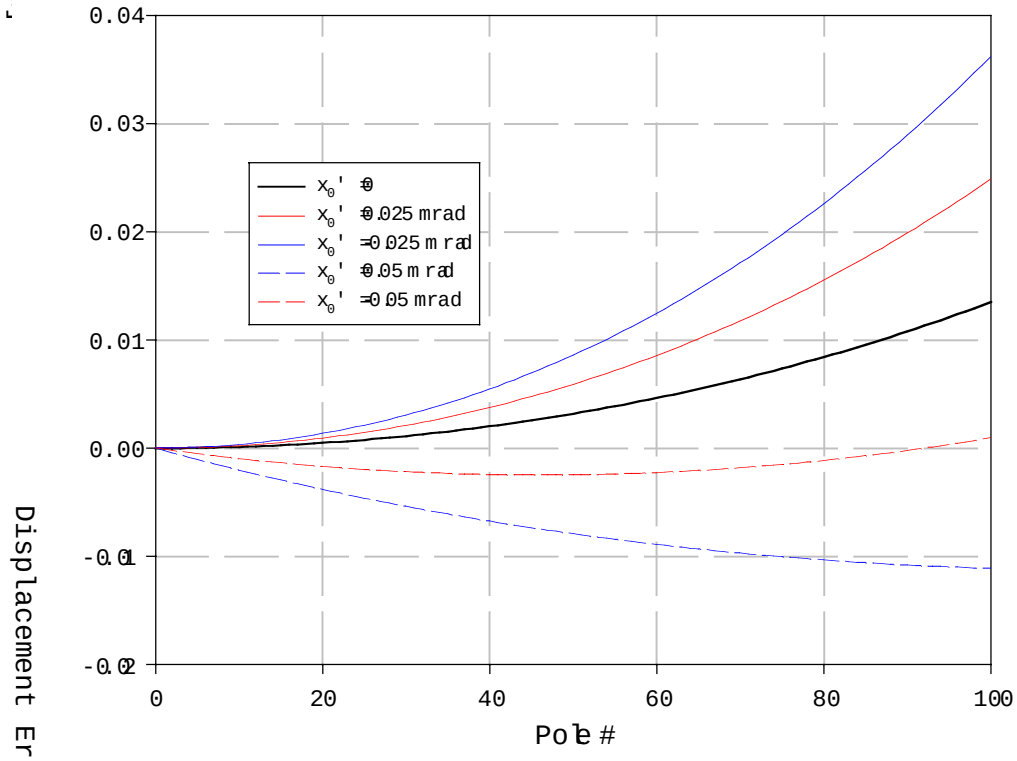

Figure 9. Trajectory deviations (cm) for pole with bumps, with $x_0 = 0$.

4.0 Vacuum system

Two options for the wiggler vacuum chamber design have been examined. The first design was for a vacuum chamber similar to that developed for the PEP-II B-factory low energy ring (LER), with continuous photon absorption on the chamber wall and a non-evaporable getter (NEG) based continuous pumping system. The second design features discrete photon absorbers and titanium sublimation pumps (TSP) to accommodate photon stimulated vacuum load, and also distributed TSP pumps in an antechamber to absorb vacuum load due to thermal outgassing.

4.1.0 NEG system - vacuum considerations

Figure 10 shows a wiggler divided into 6 period (12 pole) cells, each separated with a space for bellows, flanges, ion pumps, and a quad magnet. This layout maintains the quadrupole spacing corresponding to the physics reference design parameters (section 1.1.1). The longitudinal (beam direction) scale has been compressed in order to more clearly show the photon fan, which diverges horizontally at 13.8 mrad from the beam centerline, and its interception at various surfaces. Note that figure 10 includes photon stops which truncate the photon beam at the bellows (in the upper section), and the radiation fan extending beyond the absorber (which would be at 10 cm from the beamline center) in the lower section.

If the photon absorbing surfaces are 100 mm from center line, then the first photons hit about 7 m from the first wiggler magnet. The power hitting the chamber increases down the chamber as more magnet poles add photons. A maximum linear power density of 6 KW/m or a normal area power density of 0.6 W/mm^2 is ultimately reached. This amounts to a photon flux $6.6X10^{18}$ /s/m. 100 hour of running at the maximum power density would give a dose of $2.4X10^{24}$ photons/m, which should give a mass 28 normalized _ below $5X10^{-6}$ molc./photon, which in turn create a gas load of $9.2X10^{-7}$ Tl/s/m. To the extent that the gas loads can be predicted, the pressure profile can be made flat by tailoring the speed of the NEG pump.

Methane is normally not pumped by reactive pumps, but TSP's have been shown pump methane in the presence of photoelectrons. Methane pumping has yet to be demonstrated in NEG, but having it directly under the photon adsorber not only insures maximum conductance, but an abundance of ionizing photoelectrons. If NEG can not be made to pump methane, additional ion pumps will be needed.

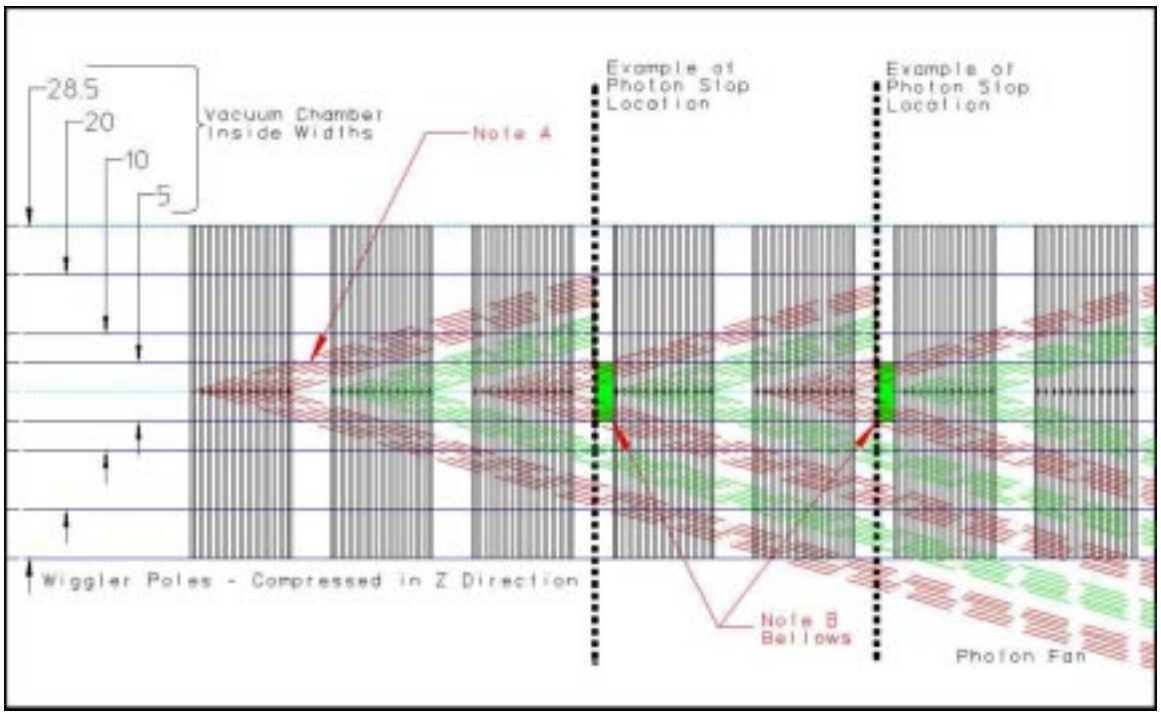

Figure 10. Anamorphic wiggler plan view showing photon fan.

4.1.1 NEG system layout

The vacuum system layout using NEG was based on the design developed for the PEP-II LER wiggler [3]. Figure 11 shows a cross-section of the vacuum chamber. The beam is contained within a circular section of 8 mm radius, the vacuum pumping section in an antechamber separated from the beam chamber by a 5 mm high and 10 mm deep slot. The slot isolates the vacuum pumping antechamber from the RF fields of the beam, thereby reducing the beam impedance of the structure. NEG material in 3 cm wide strips, approximately 1/2 mm in thickness is cut into 3 cm square wafers, which are then stacked in parallel along a stainless steel tube support. In this design, the synchrotron radiation fan generated by the wiggler is absorbed on the vacuum chamber surfaces located directly above the NEG in the pumping antechamber.

The absorbing surfaces are cooled by water passages in the walls of the vessel. The NEG material may be reactivated by a heating element contained within the vacuum sealed stainless steel support tube. The fluorescent power from the incident photons is about 600 W/m, which is low enough that the NEG can be in line of sight of the photon absorbing surfaces. Only a small amount of cooling for the NEG will be needed and will be supplied from the tube containing the heater. The NEG pump can pump 1000 l/s/m with a capacity 1.0 Tl/m, which should keep the N_2 equivalent pressure to below one nTorr.

1000 l/s/m is the maximum speed of this pump; however, lower speed with lower cost can be achieved by spacing the NEG wafers farther apart.

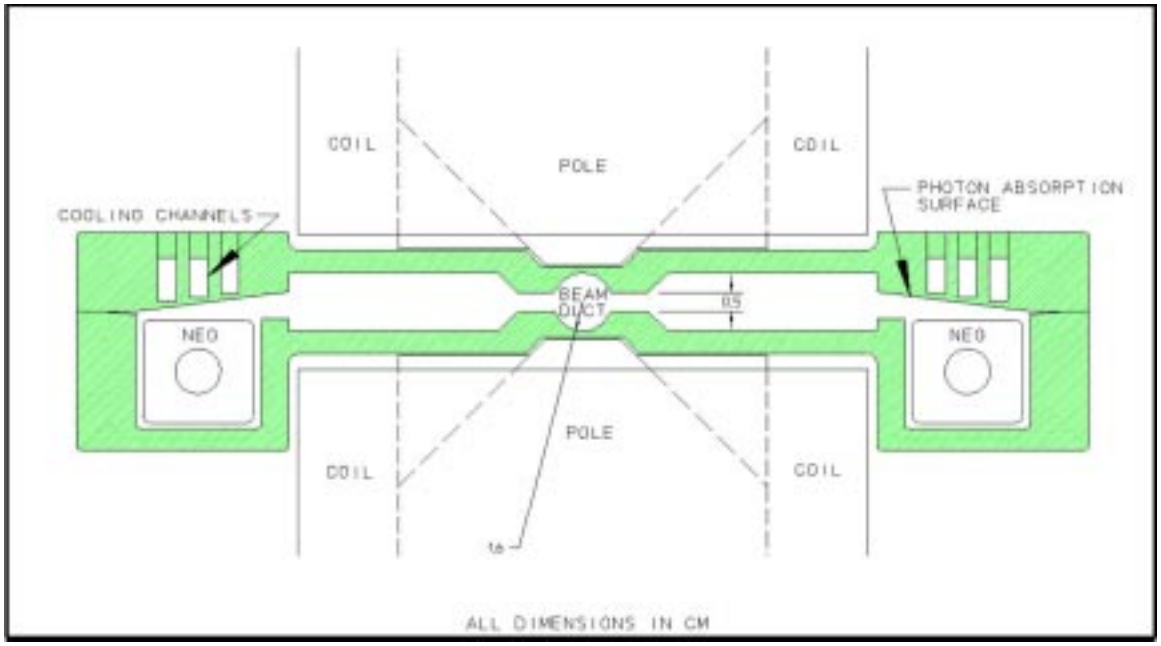

Figure 11. NEG vacuum chamber cross section.

The NEG chamber is shown in cutaway view in figure 12. An ion pump port is located just before the quadrupole magnet. In cross section, the NEG chamber is shown overlaid with a quad magnet whose cross-section is based upon an ALS design. The NEG pumping antechamber will need to be terminated to allow the vacuum chamber to pass through the quadrupole.

The raw material cost to pump a “standard 5m” wiggler chamber is about $25,000 and total pump cost is about $50,000. The attractively low power density, as compared to a discrete pump, comes at a high price in both NEG material and the very large bellow that must be used to enclose the wide photon fan.

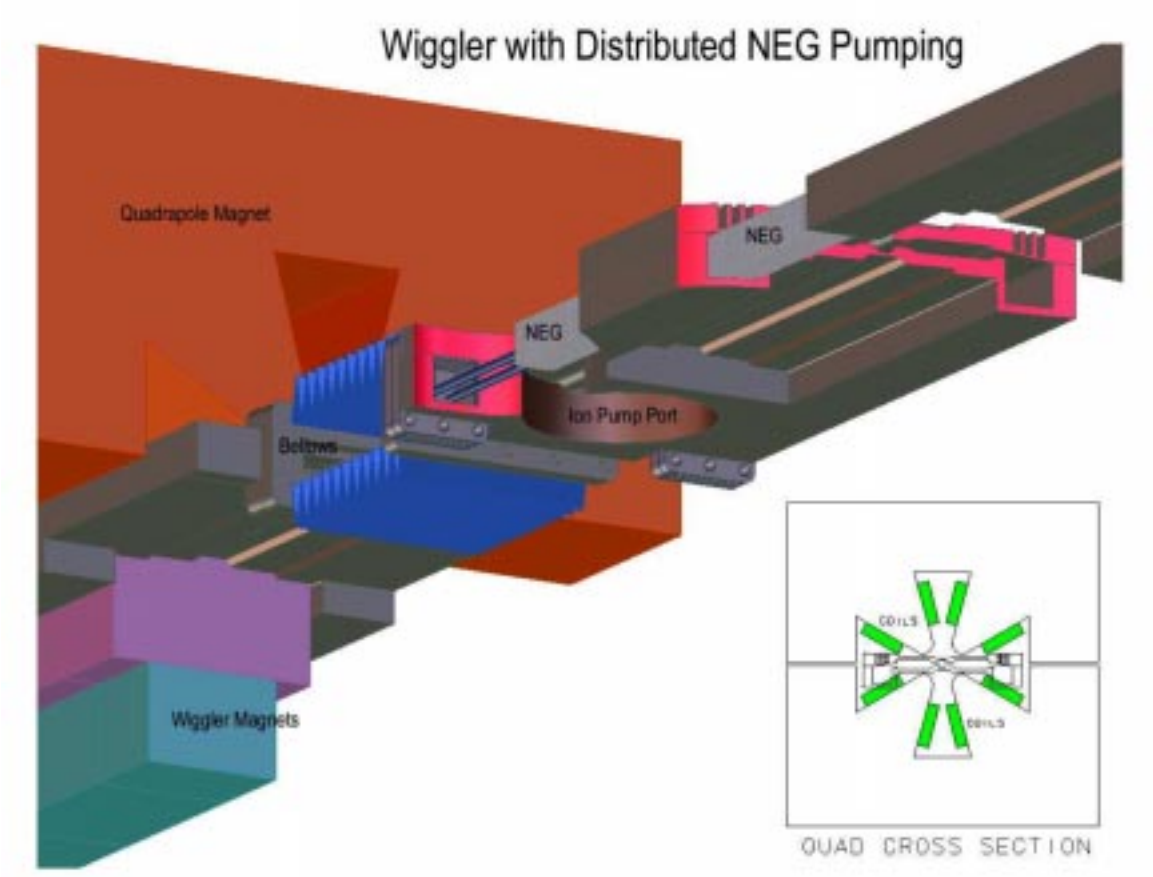

Figure 12. NEG chamber layout with cross section through quadrupole.

4.1.2 Vacuum displacement

Finite element analysis (FEA) was used to analyze the vacuum displacements of the NEG chamber under two support conditions. In both cases the chamber is assumed to be aluminum welded along its outer extent, with a 1/4" penetration weld (this is visible in the small "crack" seen in the model), and the centerline surfaces of the beam duct are constrained in symmetry. All outside surfaces of the chamber are loaded to a pressure of 101 kPa. In the first case, the upper surface of the beam duct is constrained in the vertical direction (constraints are shown by small blue arrows). In the second case, the constraints correspond to full support of the antechamber portion on upper and lower surfaces. Figures 13a and 13b show FEA results for the vacuum chamber under these conditions.

In the first case (upper surface of beam chamber constrained, figure 13a) the chamber displaces by 1.6 mm at the beam centerline - the height of the beam chamber reduces from 16 mm to 14.4 mm. In the second case (upper and lower antechamber surfaces

constrained, figure 13b) the chamber displaces by only approximately 0.25 mm per side, narrowing the beam duct from 16 mm to 15.5 mm. These two dimensional cross section models do not consider possible improvements resulting from periodic ribs placed between poles, or supports attached to the poles. In the case of a copper chamber, the displacements would be expected to be approximately one half of the values calculated for aluminum, due to the higher modulus of copper.

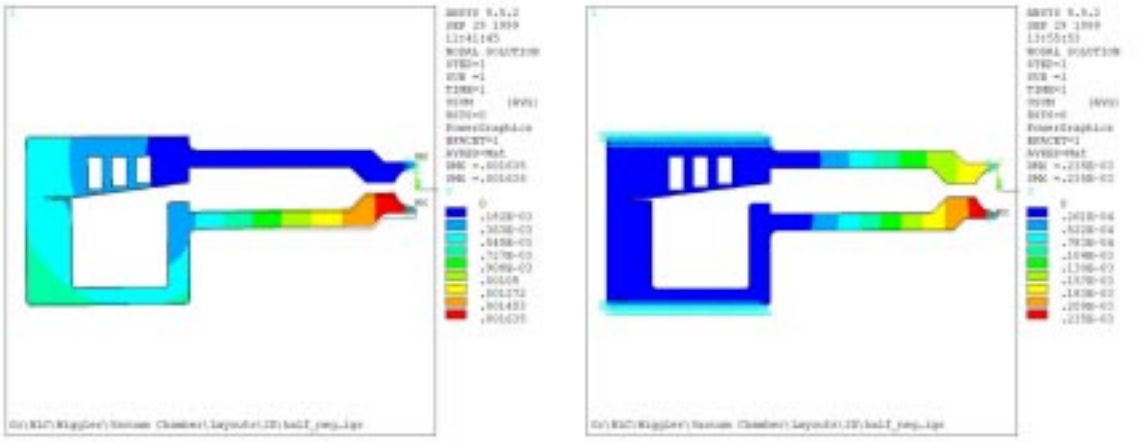

Figure 13. NEG chamber vacuum displacements.
13a (left) model constrained at top of beam chamber.
13b (right) model constrained at upper and lower surfaces of pumping antechamber.

4.1.3 Vacuum stresses

Following the same two constraint conditions described in section 4.1.2, the vacuum stresses in the aluminum NEG chamber are shown in Figure 14. For the first case (upper surface of beam chamber constrained, figure 14a) corresponding to 1.6 mm chamber deflection, a maximum Von Mises stress of 300 Mpa, or approximately 42,000 psi, is found. This stress exceeds the yield limits of many types of aluminum, and is more than half the yield of even the strongest aluminum alloy. In copper, this stress would exceed even the yield stress of work hardened OFHC. For the second case (antechamber supported, figure 14b), the maximum Von Mises stress is only 80 Mpa, or approximately 11,000 psi. Stresses of this level would be acceptable in aluminum, and perhaps in copper, depending on its working.

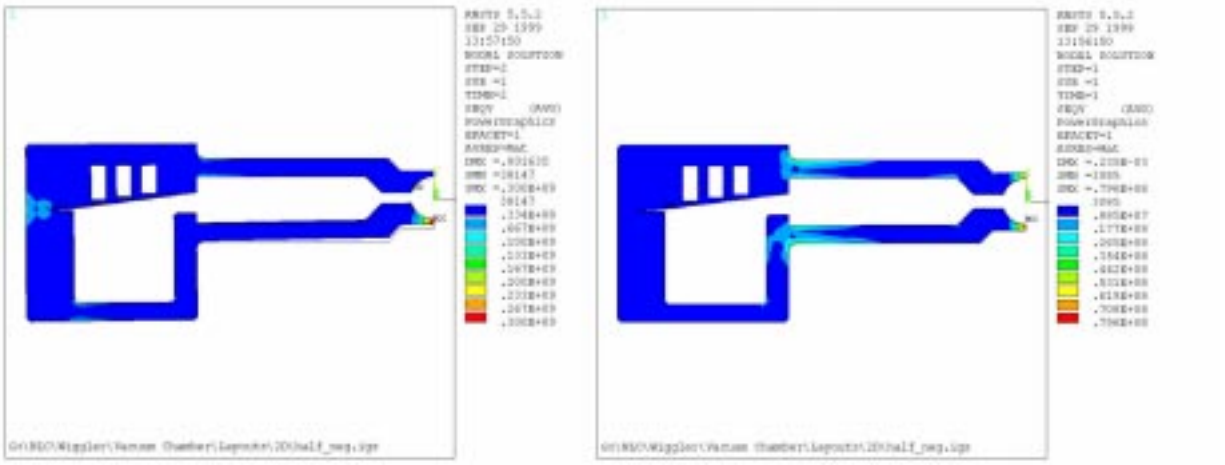

Figure 14. NEG chamber vacuum displacements.
14a (left) model constrained at top of beam chamber.
14b (right) model constrained at upper and lower surfaces of pumping antechamber.

4.1.4 Discrete photon stop requirements

Previous sections have indicated that it is difficult to pass the vacuum chamber with NEG through a quadrupole and bellows. An additional requirement is that the beam position monitors (BPM's), located in the quadrupole chamber, be below cut-off frequency for TE modes at the BPM operating frequency of 714 MHz. The cut-off for the vacuum chamber shown in figure 11 is approximately 550 MHz.

For these reasons we proposed a discrete photon stop before each quadrupole, which allows a vacuum chamber of reduced aperture to pass through the quadrupole and bellows section. With such a design in mind, the extension to a lumped titanium sublimation pump based vacuum system was made.

4.1.5 Wiggler layouts

Figure 15 shows a schematic of approximate wiggler length options. The upper layout corresponds closely to the reference design (section 1.1.1), and the lowest layout corresponds to the current baseline design (section 3.0). The other layout corresponds to wiggler sections of 12 periods each. Lengthening the wiggler cell decreases overhead associated with photon stops, quadrupoles, and bellows, and decreases the overall length of the wiggler. Also, since 160 periods are required to achieve the I_B^2 of 106 T-m^2 necessary for damping, it is important to choose a wiggler section length that is nearly

divisible into 160, in order to minimize excess length. The current option, 16 periods, produces a conservative power density on a reasonably short photon stop. Compared to the 8 period layout shown at top, the 16 period layout saves almost 8 m in total wiggler length, and 1.6 m less in quadrupole magnets. The photon beam power and height is halved in the shorter case, but the maximum normal power density at the photon absorber would be reduced only 22% because the poles nearest to the absorber contribute most to the power density.

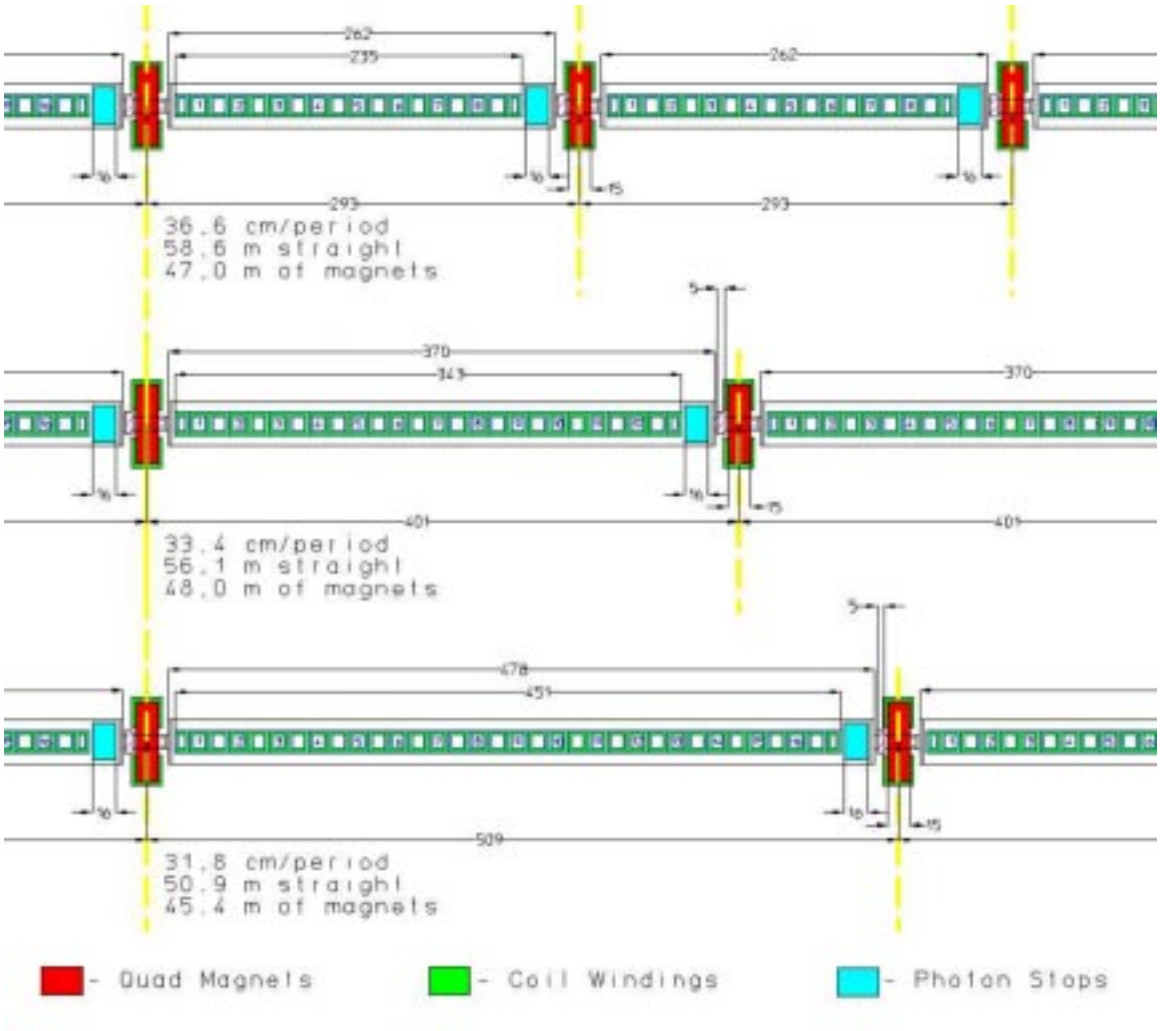

Figure 15. Wiggler layout options.

4.2.0 TSP system - vacuum considerations

In response to the considerations discussed above, a pumping system using discrete photon stops was developed. In this design the chamber and photon stop dimensions are determined such that the photon fan is intercepted at the discrete photon stops. Figure 16

shows the cross-section, which allows a simple symmetric vacuum chamber, simplifying machining or extruding.

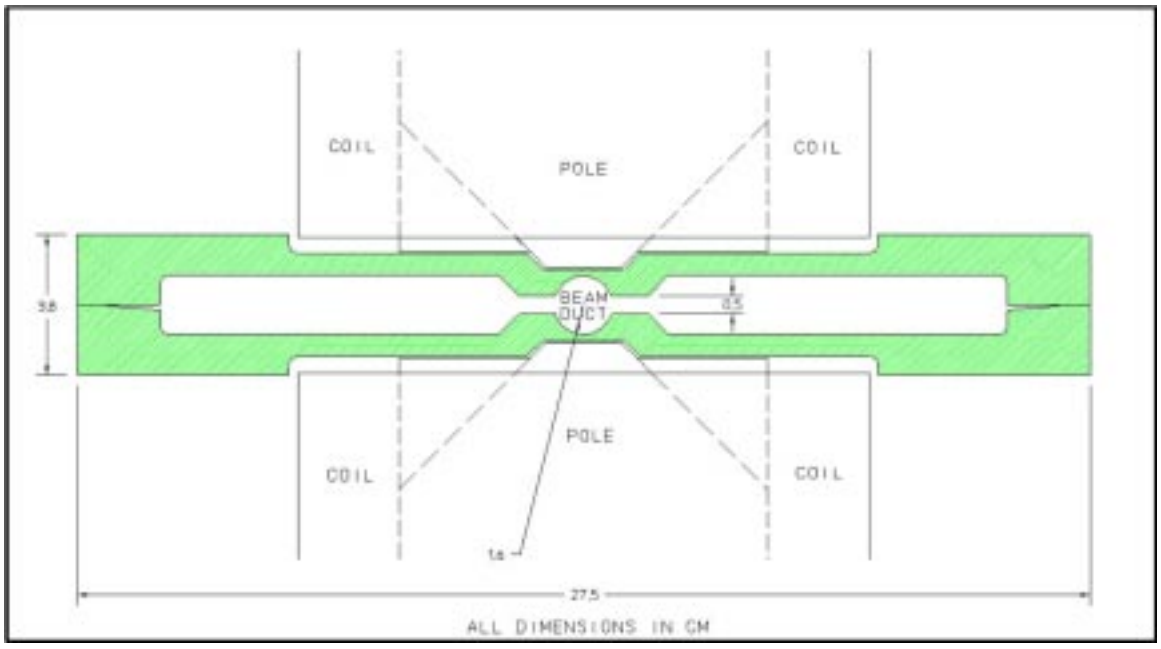

Figure 16. Wiggler chamber with discrete TSP pumping.

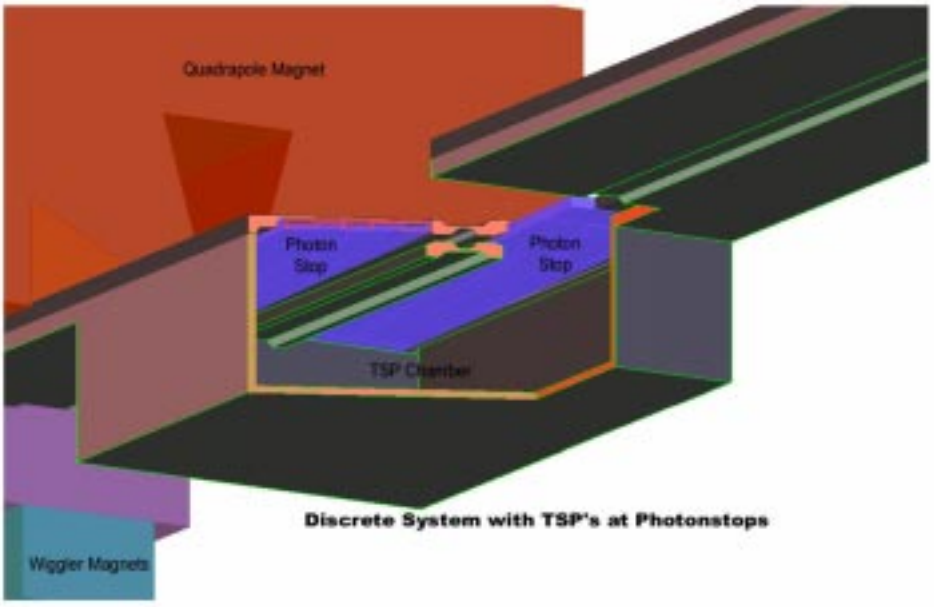

Figure 17. Wiggler layout at photon stop with lumped TSP .

This design places large TSP's beneath all photon stops in order to accommodate photon stimulated desorption. In order to pump methane and facilitate startup, ion pumps will be located adjacent to all TSP's (these are not shown). The layout is shown in figure 17.

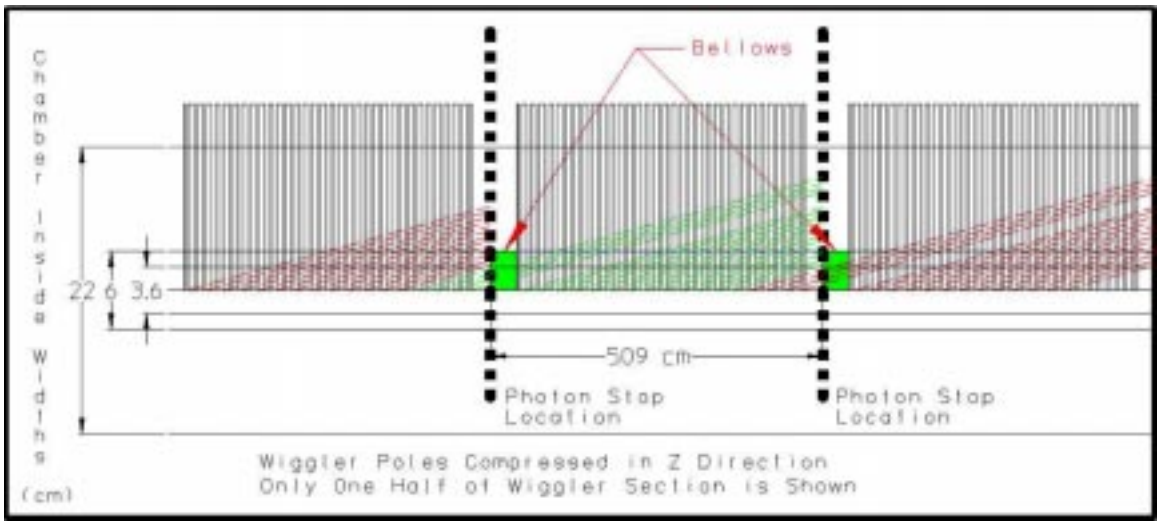

Figure 18. Anamorphic TSP wiggler plan view showing photon fan.

The baseline TSP layout of 16 wiggler periods is shown in plan view in figure 18. A photon stop situated before every quadrupole magnet. In order to prevent photons striking the vacuum chamber in the quadrupole and bellows chambers, the photon stops clip the synchrotron radiation fan down to ±18 mm from the beam centerline. This narrow aperture creates a situation where synchrotron radiation from one wiggler cell does not fall entirely on the photon stop within that wiggler chamber. This phenomenon is shown by the alternately colored photon fan lines; similarly colored lines all strike the same photon stop. It can be seen that each photon stop is illuminated by 75% of the immediate wiggler section and approximately 25% of the previous wiggler section. Interestingly, this duality causes a small gap in the illumination of the photon stop; however, this gap is on the outer end of the photon stop, where power is low, and it is not expected to cause a thermal stress problem.

Table 1 shows an estimate of the contribution of each pole to power on the inner edge of a photon absorber placed 18 mm from beam centerline. The quadrupole location is shaded, at a distance of approximately 5 m from the first pole. The nearest pole to illuminate the absorber is 1.35 m away, and the furthest to contribute significantly is 6 m. The height of the beam as shown in column F is made up of a closed orbit distortion (COD) of ±0.25 mRad and an opening angle 1/_ of ±0.25 mRad, totaling ±0.5 mRad. The

A	B	C	D	E	F
Dist-ance from pole to photon target m	Width of photon fan on absorber mm	Normal power density from each pole W/mm^2	Normal power density from all poles W/mm^2	Safe slope	Height of the beam mm
0.14					
0.27					
0.41					
0.54					
0.68					
0.81					
0.95					
1.08					
1.22					
1.35	0.68	16.597	605.3	30.3	1.4
1.49	2.6	39.1	588.7	29.4	1.5
1.62	4.4	45.2	549.6	27.5	1.6
1.76	6.3	44.8	504.5	25.2	1.8
1.89	8.2	42.1	459.7	23.0	1.9
2.0	10.026	38.6	417.6	20.88	2.0
2.2	11.89	35.1	378.9	18.95	2.2
2.3	13.76	31.8	343.8	17.19	2.3
2.4	15.63	28.8	312.1	15.60	2.4
2.6	17.50	26.1	283.3	14.16	2.6
2.7	19.37	23.8	257.2	12.86	2.7
2.8	21.24	21.7	233.4	11.67	2.8
2.97	23.1	19.8	211.7	10.6	3.0
3.11	25.0	18.2	191.9	9.6	3.1
3.24	26.8	16.76	173.7	8.7	3.2
3.38	28.7	15.48	156.9	7.8	3.4
3.51	30.6	14.33	141.5	7.1	3.5
3.65	32.4	13.31	127.1	6.4	3.6
3.78	34.3	12.38	113.8	5.7	3.8
3.92	36.2	11.55	101.4	5.1	3.9
4.05	38.1	10.80	89.9	4.5	4.1
4.19	39.9	10.12	79.1	4.0	4.2
4.32	41.8	9.50	69.0	3.4	4.3
4.90	49.8	7.40	59.5	3.0	4.9
5.04	51.7	7.01	52.1	2.6	5.0
5.17	53.6	6.65	45.1	2.3	5.2
5.31	55.4	6.31	38.4	1.9	5.3
5.44	57.3	6.00	32.1	1.6	5.4
5.58	59.2	5.72	26.1	1.3	5.6
5.71	61.0	5.45	20.4	1.0	5.7
5.85	62.9	5.20	14.9	0.7	5.8
5.98	64.8	4.97	9.7	0.5	6.0
6.11	66.6	4.75	4.8	0.2	6.1

Table 1. Estimate of wiggler photon stop parameters for discrete TSP's.

power density from each pole is shown in column C, with the pole at 1.35 m having a low density because of the extreme angle it makes to the absorber. The power density on vertical center is summed in column D. Column E shows the slope required to reduce the power density of column D to 20 W/mm^2, the maximum that we consider can be handled by water cooled absorbers.

The normal power density of the beam on centerline is an awesome 605 W/mm^2 and the full height of the photon fan would be 6 mm, but is limited by the slot to 5 mm. The power density falls off rapidly away from the vertical centerline and the inner edge of the photon absorber. The power density is half at ±0.375 mm above and below the vertical centerline, and on vertical center line the density is halved 8 mm from the inner edge. The slope of the absorber, to maintain 20 W/mm^2, on the centerline must be at least 1:30, but at the top and bottom of the absorber it can be as little as 1:0.3. A 1:30 surface that can encompass the highest density footprint is 42 mm long. The design of the photon absorber is further developed in section 4.3.

The ability of a TSP at the photon absorber to pump desorbed gases can be inferred from tests made for the ALS. Figure 19 shows the apparent pumping speed as a function of gas load of a TSP, with a 182 cm^2 inlet area and an extended condensation surface. In this test, the gas was ejected directly into the pump, as it would be under a photon absorber, and an apparent speed of 93 l/s/cm^2 or 8.5 times “black hole” speed was measured. The titanium coated surface was approximately 4000 cm^2, giving a capacity of 4X10^{-3} T*l/cm^2. This amount is equal to 50 monolayers, implying bulk pumping. Evaporative deposits made with grazing angles to a substrate are known to be porous, consistent with bulk pumping.

The area of the entrance of the TSP at the photon absorber for the wiggler would be approximately 300 cm^2 and the extended condensation surface could be 24,000 cm^2. If the speed and capacity measured in the ALS test apply, this TSP would have a speed of 28,000 l/s and a capacity of 96 T*l for all gases, except argon.

The 33 poles being examined produce 7x10^{19} photons/s and with _ of 10^{-5} the gas load will be 2x10^{-5} T*l/s. 20,000 l/s of pumping will be required to maintain a pressure of 10^{-9} Torr. Calculations indicate that 3x10^{23} photons/m will give an _ of 10^{-5} for the sum of all gases excluding hydrogen and for all gases including hydrogen a dose of 1x10^{24} photons/m will be needed [4]. This data was taken with a copper tube 3.6 m long and there may not be a direct correlation to the NLC wiggler, but the wiggler puts out 1x10^{24} photons in four hours.

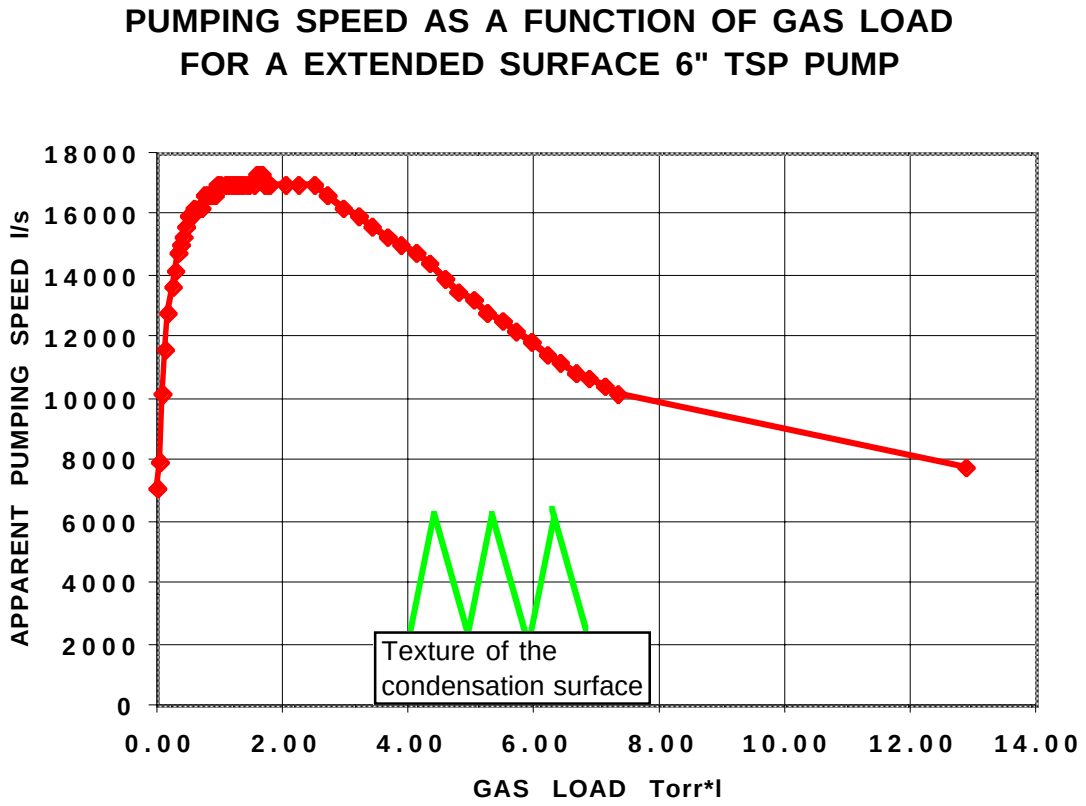

Figure 19. TSP apparent pumping speed as a function of gas load.

The 33 poles produce approximately 54 KW of synchrotron radiation. Much of this will land on the absorber, but not all of the energy will stay in the absorber - some of the photons will be spectrally reflected from grazing surfaces. Such photons will be reabsorbed on downstream steeper facets. About 3 KW is re-radiated from each absorber by fluorescence. This diffuse power goes to the TSP, and water cooling of the TSP will be required.

A vacuum chamber 5 m long would have a thermal outgassing rate of $1.2X10^{-6}$ T*l/s and at 10^{-9} T this amount to 1200 l/s. Only 10 l/s of conductance to the pumps at the photon absorbers is available, therefore distributed pumping in the antechamber is needed. NEG was examined, but without bake-out, the NEG lasts only two days before its 0.1 T*l/m capacity is consumed, as shown in Table 2.

Table 2. Pressure from thermal outgassing with distributed NEG pumping and discrete TSP's.

Pressure from Thermal Outgassing

Distance between quads m	**4.86**	**4.86**	**4.86**	**4.86**
Width mm	**230**	**230**	**230**	**230**
Height mm	**16**	**16**	**16**	**16**
Conductance from edge to center	**4436**	**4436**	**4436**	**4436**
	100% O.G.	**30% O.G.**	**10% O.G.**	**5% O.G.**
Outgassing rate Torr*l/cm2/s	**1.0E-10**	**3E-11**	**1E-11**	**5E-12**
Total outgassing for chamber T*l/s	**1.2E-06**	**3.6E-07**	**1.2E-07**	**6.0E-08**
Total pumping from NEG l/s	**438**	**438**	**438**	**438**
Average pressure from NEG Torr	**2.7E-09**	**8.2E-10**	**2.7E-10**	**1.4E-10**
Average pressure from NEG & TSP Torr	**2.6E-09**	**7.8E-10**	**2.6E-10**	**1.3E-10**
Life of NEG days	**2**	**6**	**19**	**39**

Table 2 shows the outgassing rates from unbaked aluminum ($1x10^{-10}$ T*l/s/cm^2) to baked $5x10^{-12}$ T*l/s/cm^2 and the effectiveness of two strips of NEG to manage the thermal outgassing of the vacuum chamber. Without baking, the NEG does not makes pressure goals and it lasts only 2 days. The TSP suggested by figure 19 (and figure 20) would have an extended condensation surface area of 18,000 cm^2, a conductance of 8000 l/s and a capacity of 75 T*l. This should give over one year of pumping.

In situ bake-out is useful after a water accident and could be accomplished by a heater wire parallel to the TSP wire. Free convection heat loss for the vacuum chamber at 150^{o}C is less than 600 W/m. Two 3.2 mm wires made of 80%Ni-20%Cr will radiate 600 W/m with 46 A and stay below 900 ^{o}C. The transverse thermal gradient, under these conditions, is less than 15^{o}C. A hot water system, as used by APS, may also be considered, as may wrapping the vacuum chamber in heating jackets and thermal insulation.

4.2.1 TSP system layout

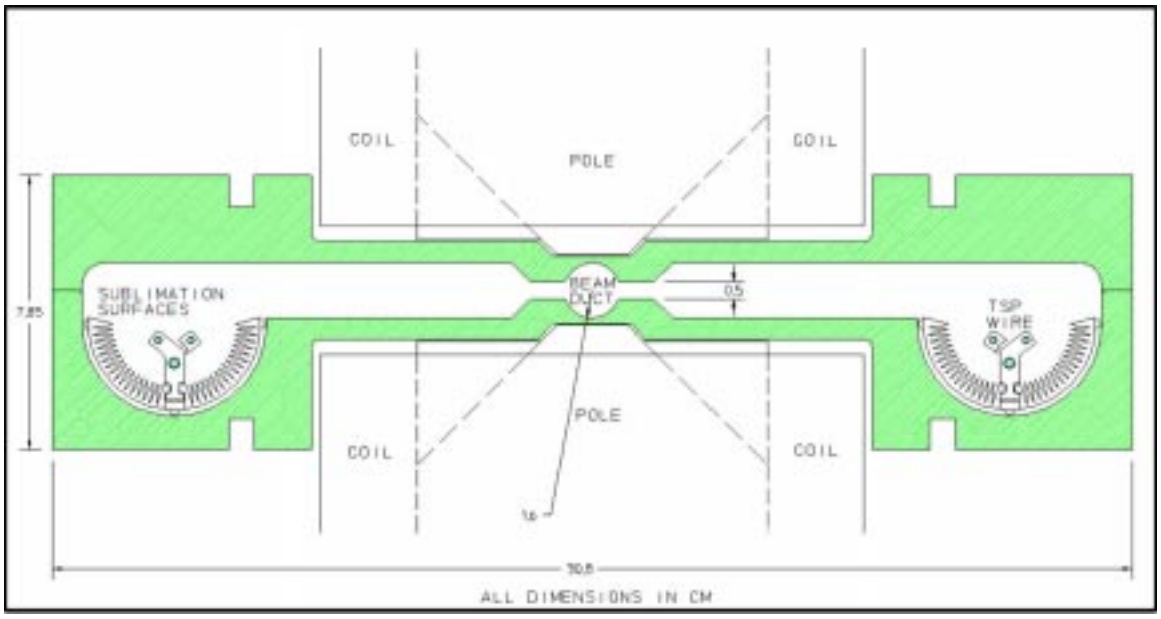

Figure 20. Distributed TSP pumping.

Figure 20 shows a design which incorporates a TSP cartridge inserted into the vacuum chamber. The cartridge consists of a filament, support, and pumping surface, with the titanium wires suspended opposite the sublimation surface. This distributed pumping is for thermal outgassing only, there is no photon desorption on these surfaces.

4.2.2 Vacuum displacement

Finite element analysis (FEA) was used to analyze the vacuum displacements of the TSP chamber under two support conditions. In both cases the chamber is again assumed to be aluminum welded along its horizontal centerline, with a 1/4" weld penetration. Figure 21 shows the chamber cross section at the discrete pumps under atmospheric loading, in conditions directly analogous to those of sections 4.1.2 and 4.1.3. For the first case (upper surface of beam chamber constrained, figure 21a) the chamber displaces less than its NEG counterpart, but still a considerable 1.3 mm. The benefit of constraining the chamber outside of the wiggler magnets is seen again (figure 21b), as it reduces the overall displacement to less than .2 mm *per side*, or .4 mm overall. While this chamber performs better than its NEG counterpart, it does not perform well enough to alleviate the need for significant support.

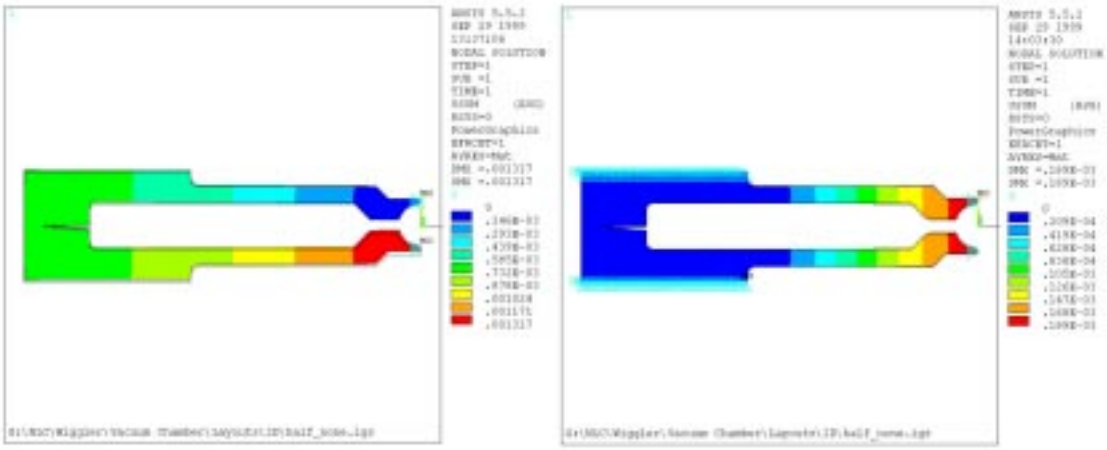

Figure 21. Discrete TSP chamber vacuum displacements.
21a (left) model constrained at top of beam chamber.
21b (right) model constrained at upper and lower surfaces of pumping antechamber.

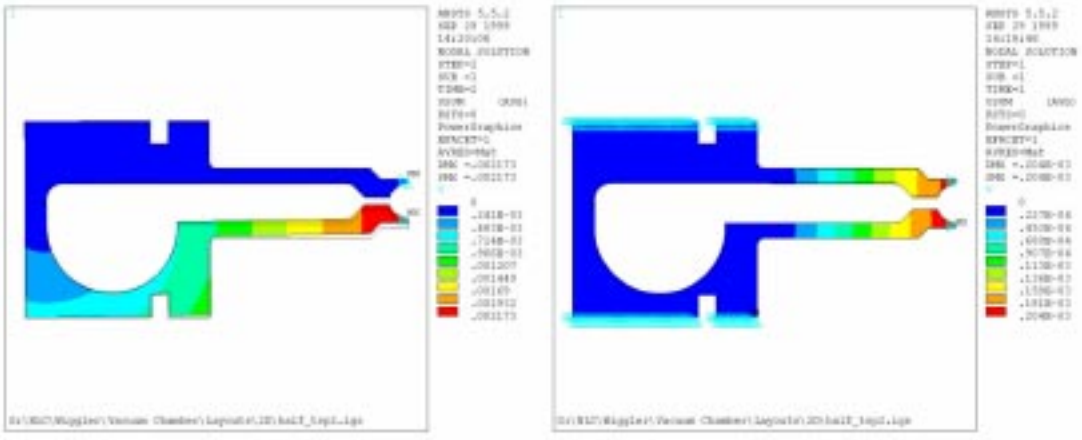

Figure 22. Distributed TSP chamber vacuum displacements.
22a (left) model constrained at top of beam chamber.
22b (right) model constrained at upper and lower surfaces of pumping antechamber.

Figure 22 shows the vacuum displacements in the chamber with distributed pumping under atmospheric loading. With the upper surface of the beam chamber constrained, figure 22a, displacements of 2 mm are found, similar to that seen with the NEG chamber cross sections, and due to large cutouts in the cross section for the TSP sublimation

surfaces. With the antechamber supported, figure 22b, we find displacements of 0.2 mm per side.

The deflection of the chamber may be reduced by pre-forming the chambers to compensate for the vacuum deflection. For example, if the chamber deflection under vacuum load is 0.2 mm, the chamber can be fabricated to be +0.2 mm oversize. The chamber will be held in place by the magnet poles, and stresses partially relieved after pump-down.

4.2.3 Vacuum stresses

Following the same two constraint conditions described above, the stresses in the TSP vacuum chamber were calculated and are shown in figure 23 for the vacuum chamber at the discrete pumps. Von Mises stresses in the first case (upper surface of beam chamber constrained, figure 23a), are slightly less than 140 Mpa, or 20,000 psi, - less than half that of the free NEG chamber, due to the elimination of the flexible NEG "cutout" in the chamber cross section. The stresses in the second case (antechamber supported, figure 23b), however, are very close to those seen in the NEG chamber, at approximately 75 Mpa, or slightly under 11,000 psi. This result is to be expected, since the NEG and discrete chambers share an identical cross section inboard of the support area.

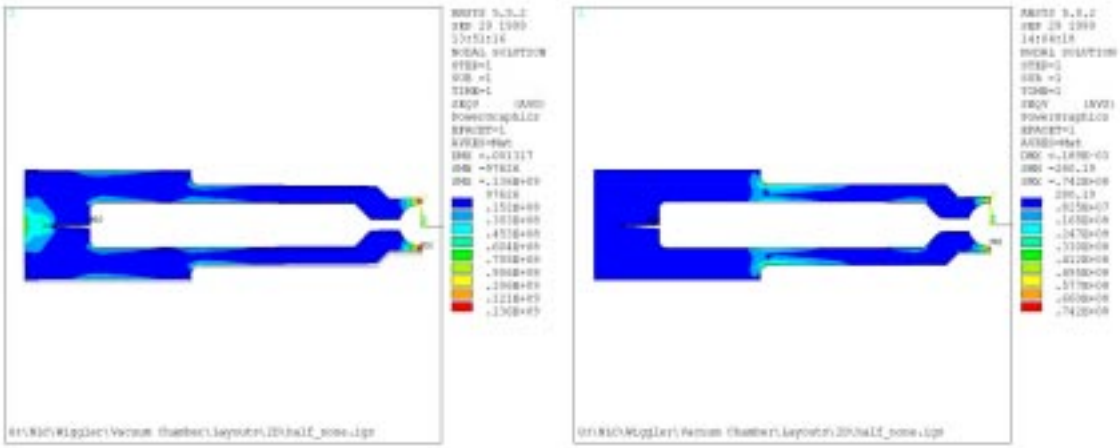

Figure 23. Discrete TSP chamber vacuum displacements.
22a (left) model constrained at top of beam chamber.
22b (right) model constrained at upper and lower surfaces of pumping antechamber.

Figure 24 shows the case for the distributed TSP vacuum chamber. Both constraint conditions exhibit behavior similar to the NEG chamber (section 4.1.3). Stresses are high

on the lower side of the chamber in figure 24a, approximately 40,000 psi, and much lower in figure 24b, approximately 11,000 psi, distributed evenly between the top and bottom halves of the chamber.

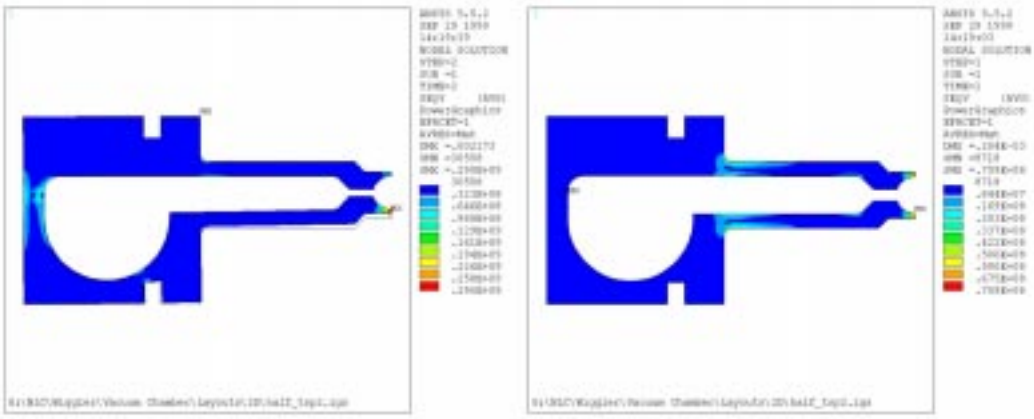

Figure 24. Distributed TSP chamber vacuum displacements.
24a (left) model constrained at top of beam chamber.
24b (right) model constrained at upper and lower surfaces of pumping antechamber.

4.2.4 Wire sag during sublimation

Although sublimation is performed infrequently and for short periods of time, it is critical that the TSP wire, which is resistively heated, not touch the surrounding chamber or support structure. Typically, sublimation cycles run at 1000°C, and an analysis of the wire sag at this temperature was performed. The TSP wire was assumed to have a constant coefficient of thermal expansion of 10 ppm/°C, corresponding to the coefficient of thermal expansion for pure titanium at 1000°C. This is an approximation for TSP wire composed of 85% Titanium and 15% Molybdenum.

The wire sag was calculated assuming that the wire can take no strain in its axial direction, and that any thermally induced elongation results in sag, and the supports were assumed to be fixed in position. Furthermore, the deformed shape of the wire was approximated as a perfect caternary. Figure 25 shows the wire sag as a function of support spacing (both in cm). It is evident that the wire sag is substantial, and will require supports at intervals of less than 10 cm.

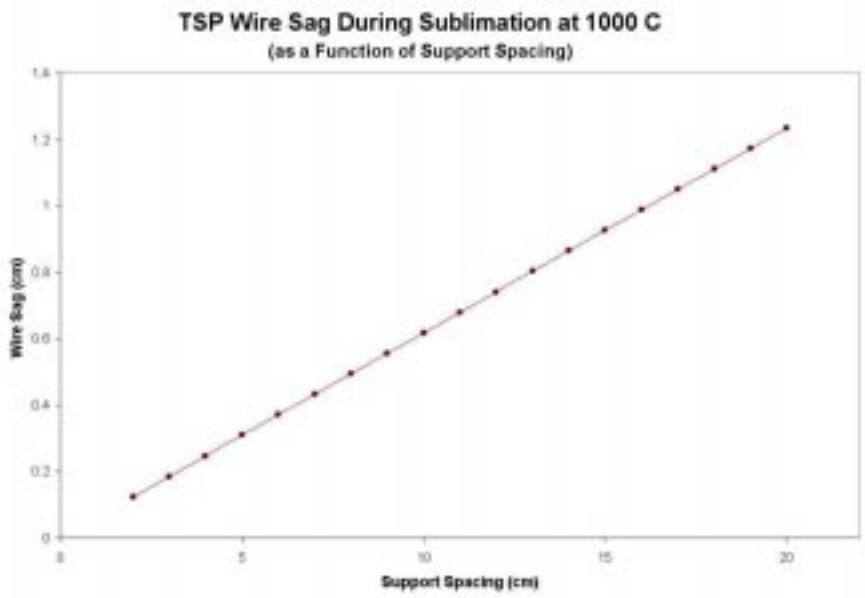

Figure 25. TSP wire sag during sublimation.

4.3 Discrete TSP photon stop

The wiggler vacuum system is designed so that each wiggler section illuminates two photon stops, one on either side of the beam duct. Each stop is positioned so that its inside edge is located 18 mm from the beam centerline, at the edge of the available aperture. Figure 26 shows the normal power distribution at the photon stop, as a function of vertical position and distance from the beam centerline. The chamber slot is 5 mm tall, limiting the maximum possible height of the photon fan. The peak power density is approximately 650 W/mm^2, while the total absorbed power is 19 kW per photon stop.

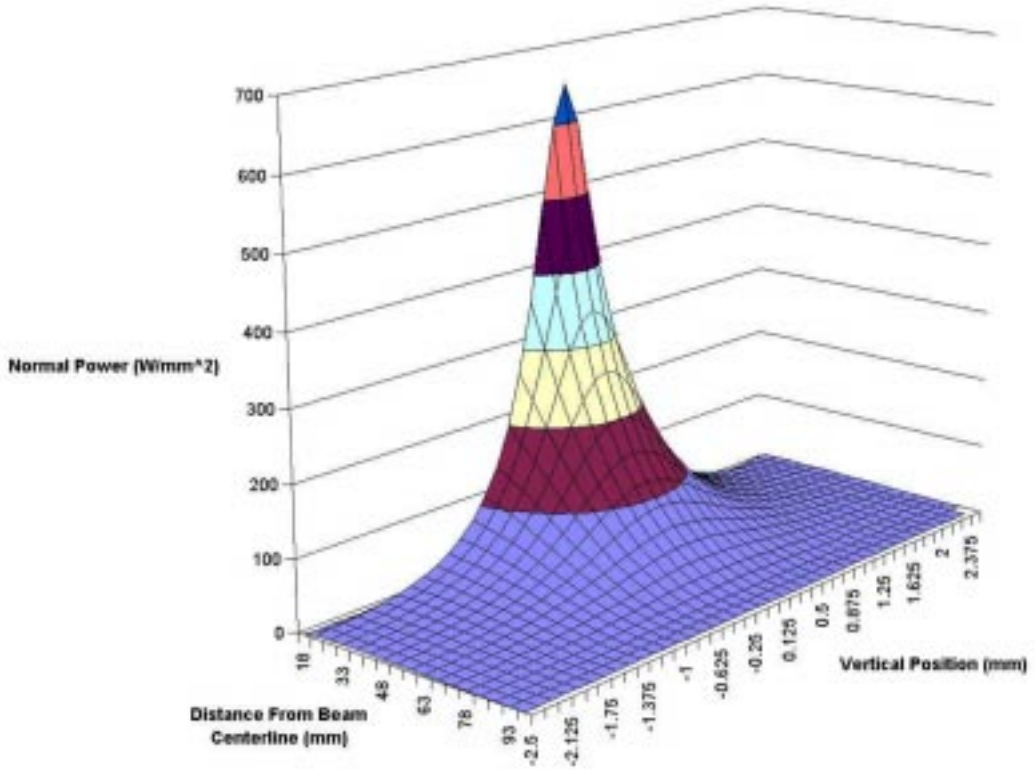

Figure 26. Normal power loading at photon stop as a function of vertical position and transverse distance from beam centerline.

To reduce power density on the absorber surface, the photon stop is designed with a shallow absorbing angle relative to the beam direction. This angle, approximately 65:1, is chosen so that the maximum power does not exceed 10 Wmm^{-2}, a conservative design goal. By faceting the stop, it is possible to absorb all of the incident power, and to maintain the power density below 10 Wmm^{-2} with a reasonably short stop. Adding facets, however, results in large changes in the power density for mis-steered beams.

The incident power on the photon stop (along its inner edge, versus vertical position) is shown in figure 27. This distribution is computed for a simple photon stop with just three facets: one low-angle center facet, and two steeper, shorter end facets. The facet lengths are determined by optimizing the stop for the shortest possible length while retaining the design power of 10 Wmm^{-2}. The effect of misteer is also shown in this figure, with .05 mm and .25 mm vertical offsets shown. It can be seen that a .25 mm vertical misteer, only 5% of the slot height, results in a maximum power increase of more than 80%. The peak power density, however, remains below 20 W/mm^{-2}, which we consider an acceptable worst-case power density. A 50 micron misteer, on the other hand, increases power intensity by little more than 10 percent.

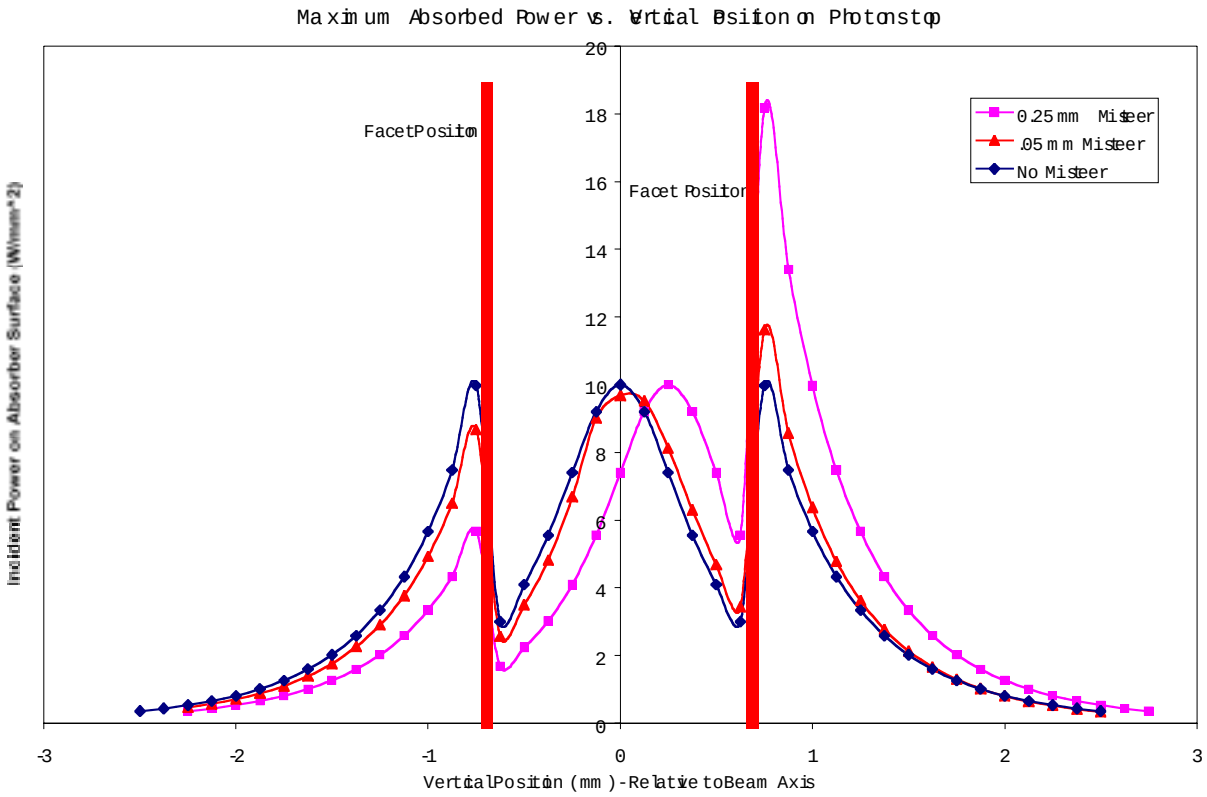

Figure 27. Power loading on faceted photon stop with one central facet and two steeper, outer facets. Both nominal and offset (beam misteer) loadings are shown. Red bars indicate boundaries of facets.

Having defined the facet locations, it is necessary to define the cooling scheme. Utilizing the standard approach of rectangular channels separated by thin "fins", a photon stop design was created with the concept of machining the geometry from a solid piece of Glid-Cop. In order to facilitate machining operations, the cooling grooves are chosen so that they have straight bottoms; this choice results in variations of the distance from the absorbing surface to the cooling channel, the "hotwall", as a function of position. The channel placement shown in Figure 28 was chosen so that the minimum hotwall thickness never falls below 1 mm, while the maximum hotwall thickness never exceeds 2 mm. In addition, the channel period is chosen based on extensive 2-d theoretical calculations of different photon stop fin designs. In these analyses, it was discovered that the optimum fin/period ratio is between 50 and 60 percent. The channel height was chosen using similar analytical considerations. The photon stop overall dimensions are based on the size and height of the incoming fan, with an additional 10 mm "manifold" area added onto each end. For simplicity, the water channels are shown projecting through the entire stop.

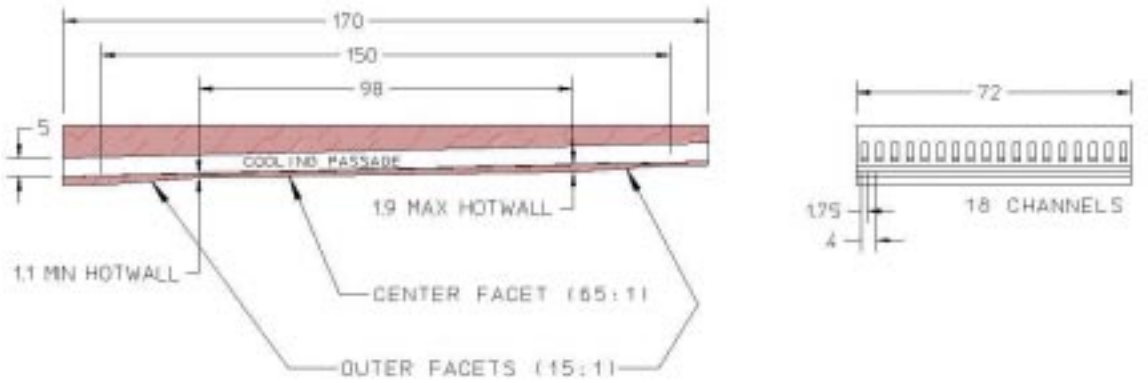

Figure 28. Photon stop layout with cooling channel section view.

A finite element analysis model of the photon stop was created in ANSYS. The mesh consists entirely of bricks, with a variable size, and a total of approximately 80,000 elements. The heat flux loads shown in figure 26 were transferred in tabular format. Two loading cases were examined: nominal, with a maximum of 10 Wmm^{-2}; and offset, corresponding to a 0.25 mm vertical misteer. The heat flux loads for the two cases are shown in Figure 29. Both the nominal and offset models were analyzed using convection constraints on the cooling passage walls, with a heat transfer coefficient of 35,000 $W/m^{-2}K$. This convection condition corresponds to a flow rate of 20 feet per second, and a Reynolds number of 22,000. Coolant temperature was set to zero, so that all temperature values given are in °C above water temperature. Since fairly high stresses are anticipated, the material was chosen to be Glid-Cop.

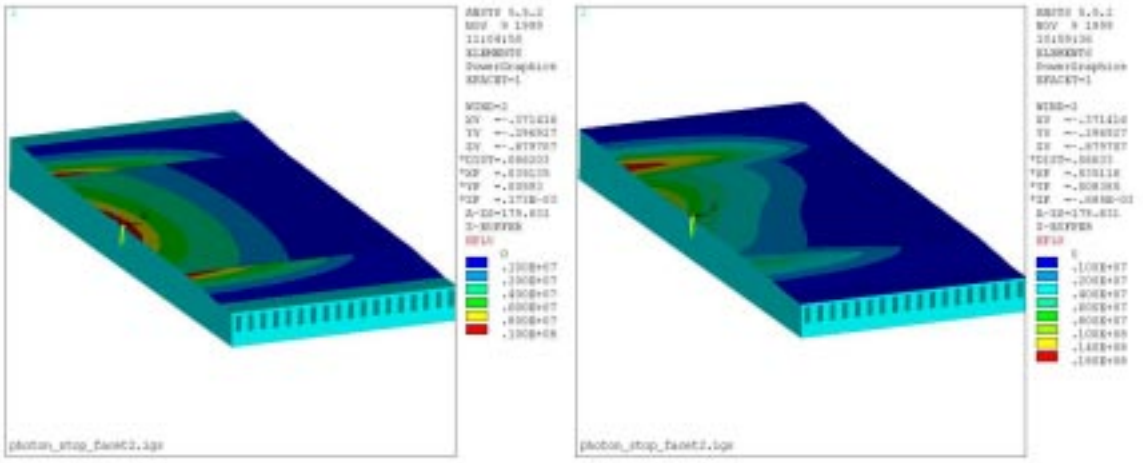

Figure 29. Power distribution on photon stop.
29a (left) Power distribution (Wm^{-2}) on photon stop during nominal operation.
29b (right) Power distribution on photon stop during 0.25 mm vertical misteer.

The thermal analysis solutions are shown in Figures 30 and 31, for the nominal and offset cases, respectively. For the nominal operation case, the maximum surface temperature is found to be 144 degrees above coolant, or approximately 175 degrees Celsius, assuming a 30 degree water supply. For the offset case the temperature increases, but predominantly over a small area at the junction of the two facets; its maximum temperature is 222 above coolant, or approximately 250 degrees Celsius.

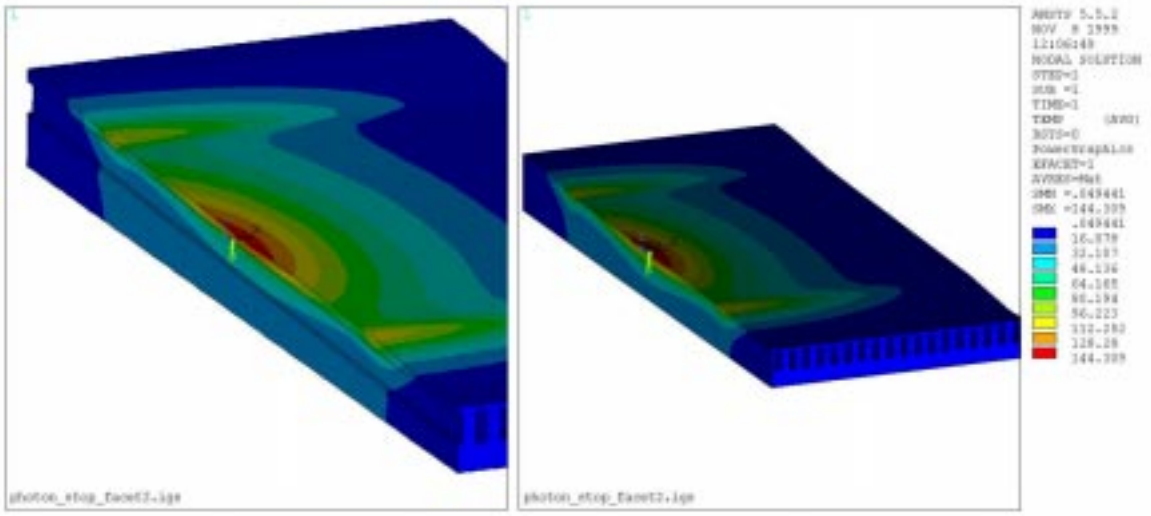

Figure 30. Temperature distribution on photon stop during nominal operation. Values are °C above water temperature; cutaway view of first water channel is shown at left.

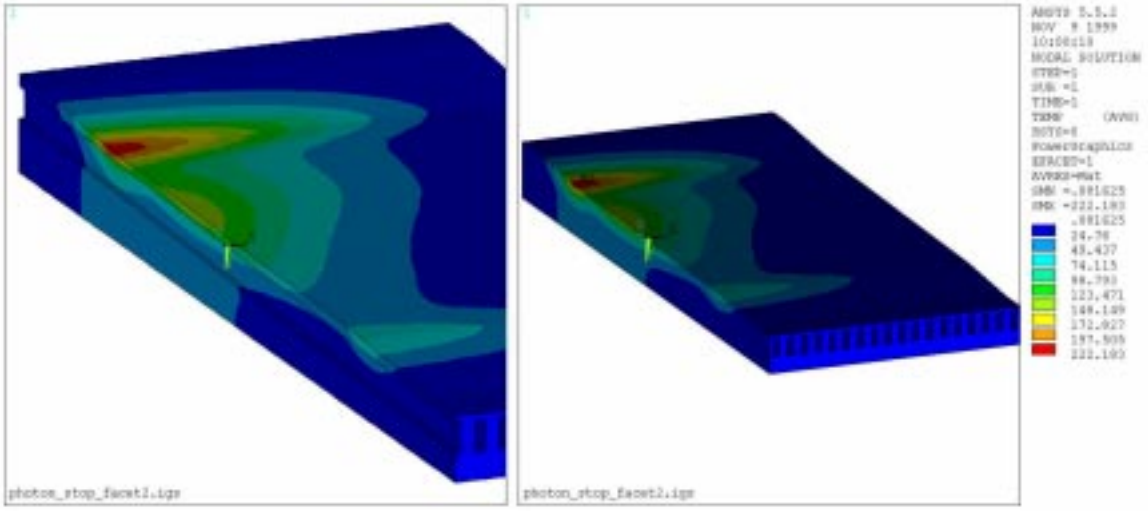

Figure 31. Temperature distribution on photon stop during 0.25 mm vertical misteer. Values are in °C above water temperature; cutaway view of first water channel is shown at left.

The water surface of the water channel, or wetwall, temperature, however, is more critical than the surface temperature of the stop, since this temperature defines the pressure of the coolant supply to prevent boiling. For the nominal case, the wetwall temperature is approximately 160 degrees Celsius, while for the offset case this temperature increases to almost 200 degrees Celsius. In order to safely withstand operation in the nominal condition, the water supply must be approximately 75 psi gauge. For the offset case, this pressure requirement increases to 235 psi gauge. However, boiling does not occur in a water supply immediately when the wetwall temperature reaches its boiling point, so it may not be necessary to run at such a high pressure in order to safely guard against temporary excursions into offset loading operation. Photon stop functioning under these and other, more extreme conditions will be explored further in the future.

In order to quantify the effect of coolant temperature change along the water passages, the FEA model was used to compute the total heat lost in the hottest (inside) water channel. For both load cases this heat loss is approximately 2.6 kW. Considering a flow rate of 20 fps, a simple energy balance on the water passage gives a temperature rise of approximately 12°C along the channel. This is small compared to the temperature of the surface, so its effect may be neglected. However, if the channels are configured to run in a serpentine fashion then this temperature rise will become important.

While wetwall temperature is critical to the photon stop's safety, its stress state is also very important. Thermal loading cases for an on-axis beam and a 0.25 mm offset were used in order to calculate thermally induced stresses in the stop, see Figures 32 and 33. In each situation, the stop was kinematically constrained such that it could bend freely in both directions. In actuality, the stop may be more fully constrained than this approximation, and these constraints will need to be evaluated. For the nominal load case, the maximum stress in the stop was computed at approximately 160 Mpa, or 23,000 psi. Considering that Glid-Cop exhibits a yield strength of 60,000 psi, the factor of safety for stress is a little more than 2.5. For the offset case, the maximum stress increases to about 240 Mpa, or 34,000 psi, leaving a factor of safety of 2. Since these peak stresses occur over a small area, and are localized to the surface of the stop, operating periodically at levels of up to 35,000 psi should not pose a problem from the stress perspective.

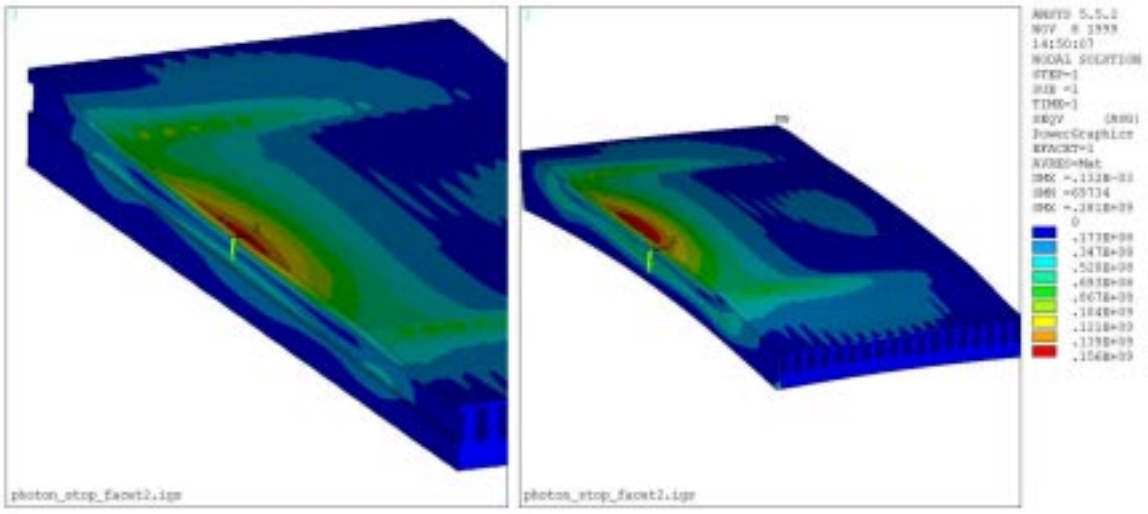

Figure 32. Stress distribution on photon stop during nominal operation. Values are Von Mises stress in Pascals.

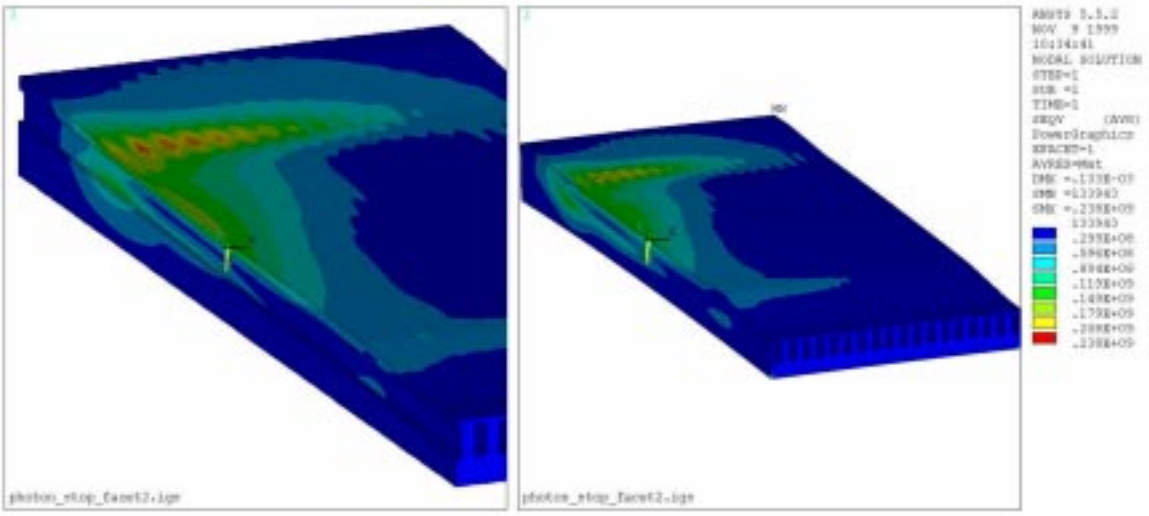

Figure 33. Stress distribution on photon stop during 0.25 mm vertical misteer. Values are Von Mises stress in Pascals.

One photon stop concept is presented here, although other designs have also been under consideration. One possibility is a photon stop that exhibits a continuously curved absorbing surface, in order to equalize the power more efficiently, resulting in reduced stop length. A curved design may also allow safer operation under offset loading, since it does not contain any discreet changes in slope which can cause significant load magnification, as shown above. In addition to this curved design, the benefit of adding

crenelations to the absorbing surface is also being examined. Although crenelations may increase temperature and stress slightly on the vacuum side, they are efficient at reducing wetwall temperatures significantly, if this should become necessary. The photon stop described here is considered to be a viable working design, but it needs to be examined more carefully in respect to beam mis-steer. Other means of accommodating beam mis-steer may be necessary, such as dynamic positioning, and these will be examined in the future.

5.0 Baseline wiggler layout

The layout shown in Figure 34 consists of a wiggler with 16 periods, in addition to approximately 1/3 period at each end, and one photon stop, in a single chamber. This chamber joins to a bellows which couples to a smaller chamber of 6 cm full width. The smaller chamber incorporates the BPM, and passes through the quadrupole magnet, to connect to another wiggler section on the other side. Pumping consists of a lumped TSP at the photon stops, in addition to an ion pump, and a distributed TSP system as described above. The cut-off frequency of TE modes in the smaller chamber is 2.86 GHz, and the attenuation constant at the BPM operating frequency of 714 MHz is 58 m^{-1}, resulting in 25 dB attenuation in a length of 5 cm.

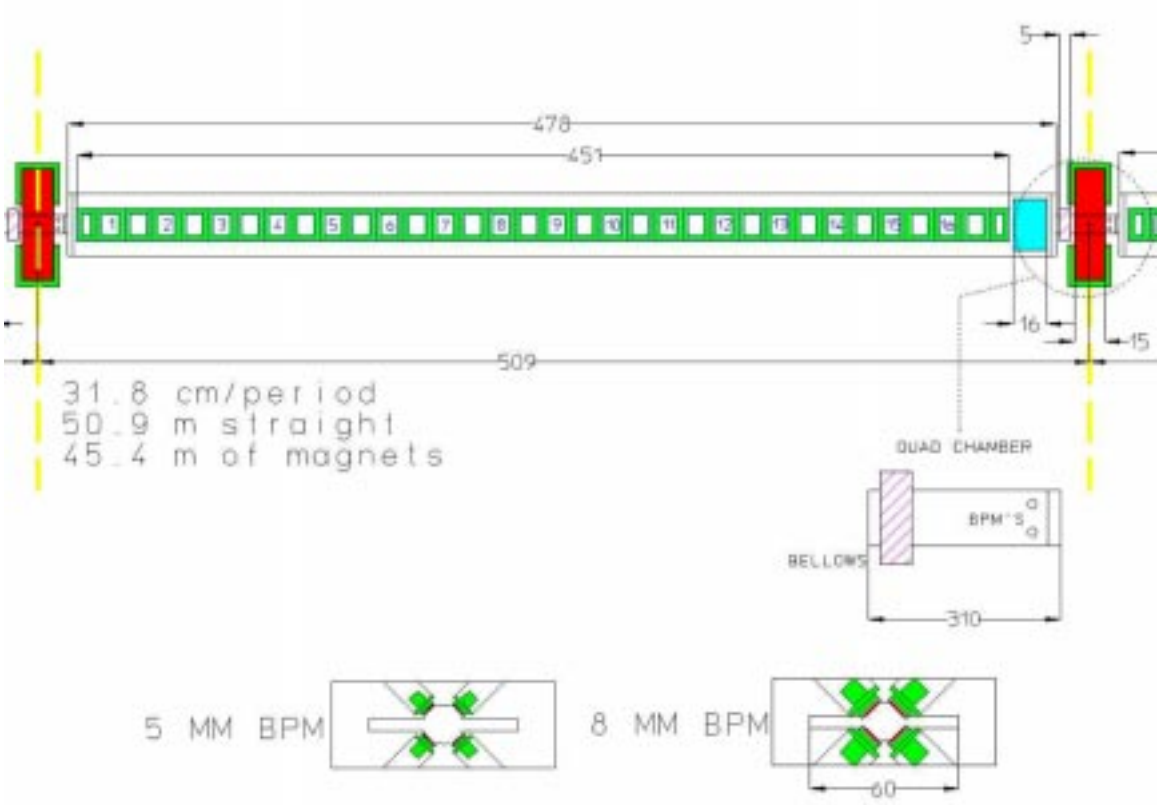

Figure 34. Plan layout of baseline design with TSP vacuum system.

References

[1] P. Emma, T. Raubenheimer, “Preliminary main damping ring design for the NLC” SLAC Memorandum, April 23, 1999.

[2] Zeroth-order Design Report for the Next Linear Collider, Chapter 4, LBNL-PUB-5424, SLAC Report 474, UCRL-ID-124161.

[3] L. Bertolini et. al. "Design of the linear non-evaporable getter pump for the PEP-II B-factory", Proc. 1997 Particle Accelerator Conference, Vancouver, May 1997.

[4] Grobner et al, J. Vac. Sci.Technol. A 12(3), May/Jun 1994.